Numerical Simulation Of Bubble Screens For Mitigating Salt Intrusion Through Sea Locks

Kesong Feng

Master of Science Thesis

TU Delft Delft University of Technology

Process & Energy

Numerical Simulation Of Bubble Screens For Mitigating Salt Intrusion Through Sea Locks

Master of Science Thesis

P & E report number 3001

For the degree of Master of Science in Energy & Process Technology at Delft University of Technology

Kesong Feng

Supervisors:
Dr.ir.W.-P. Breugem
Dr.ir. M.J.B.M. Pourquie

November 27, 2019

Faculty of Mechanical, Maritime and Materials Engineering (3mE) · Delft University of Technology

The work in this thesis was supported by Hydraulics for Infrastructure and Industry Group, Deltares. Their cooperation is hereby gratefully acknowledged.

Delft University of Technology
Department of
Process and Energy (p&E)

The undersigned hereby certify that they have read and recommend to the Faculty of Mechanical, Maritime and Materials Engineering (3mE) for acceptance a thesis entitled

Numerical Simulation Of Bubble Screens For Mitigating Salt Intrusion Through Sea Locks

by

Kesong Feng

in partial fulfillment of the requirements for the degree of

Master of Science Energy & Process Technology

Dated: November 27, 2019

Supervisor(s):

Dr.ir.W.-P. Breugem

Dr.ir. M.J.B.M. Pourquie

Reader(s):

Dr.ir. G.H. Keetels

Abstract

Salt intrusion through sea locks causes the mixing of fresh and salt water due to a gravity current. This process may occur gradually over tens of kilometers and affects the required quality of the inland water. A bubble screen alongside the locks is one of the available mitigating measures for this undesired phenomenon. However, current numerical simulations on bubble screens to mitigate salt intrusion are relatively scarce, and the validation of such models has not yet been thoroughly checked. The objective of this thesis is to study the performance of bubble screens for mitigating the salt intrusion using an Euler-Euler Computational Fluid Dynamics (CFD) model in Fluent 17.2. The work was conducted at TU Delft in collaboration with Deltares, a hydraulics institute in Delft in The Netherlands.

First, a simulation of a gravity current is conducted to study the mixing of fresh and salt water in the absence of a bubble screen. The mass transport equation for the salt concentration, together with a linear approximation of the concentration-density relation, is involved into the governing equations. The results are validated with empirical predictions and experiments at Deltares of gravity currents to study the buoyancy effects of different turbulence submodels.

Second, simulations of bubble screens in the fresh-fresh water system are performed and validated with particle image velocimetry (PIV) measurements conducted at Deltares to investigate the bubble screen dynamics. Larger flow circulations are generated with increasing air flow rates, while a constant surface current thickness of around 0.3 times the water depth is found for all cases.

Lastly, bubble screens simulations for six different Froude air numbers Fr_{air} in the fresh-salt water system are conducted and validated with the dye measurements. The dimensionless number Fr_{air} serves as a ratio of the kinetic energy of the rising bubble plume to the potential energy of the gravity current. The salt transmission factor, defined as a ratio of the salt intrusion with mitigating measures to that without any measures, shows that Fr_{air} in the range of 0.93 - 1.08 is most efficient for mitigating salt intrusion. At a lower Fr_{air}, the salt water generally intrudes at the bottom area as a salt tongue, whereas the salt intrudes through the surface current for larger Fr_{air} owing to a higher rate of liquid entrainment into the bubble screen.

Table of Contents

List of Figures

List of Tables

Acknowledgements

I would like to thank my supervisor Dr.ir.W.-P. Breugem for guiding and supporting me throughout my thesis project. His guidance has helped me understand better about the basic theories and further inspired me continuously on thinking and writing. I would also like to express my gratitude towards my another supervisor Dr.ir. M.J.B.M. Pourquie for providing his valuable support and advice in handling with the simulations. Discussions with him not only helped me solve the problems in a more practical way, but also passed through the optimism to me.I would also like to express my thanks to the committee members for devoting their time and effort in evaluating my thesis report.

I am grateful to Tom O'Mahoney at Deltares for helping me understanding the project and providing continuous support on the relevant work and measurements. I am also thankful to Arthur Oldeman and Thomas Flint for offering insightful advice and recommendations every time I got stuck. Also, I would like to say thanks to Shravan Raaghav and Kishan Kumar for the interesting talks we have had about the project and further plan.

I am thankful to all my friends for constantly motivating and helping me during my stay here in Delft, especially to my classmates and roommates Xihe Li, for supervising me to have a regular and healthy basis of study and life.

Last, but not the least, I express my deepest gratitude to my family for showering their love and support on me always. Their faith in me has been a constant source of inspiration for me.

Delft, University of Technology — Kesong Feng
November 27, 2019

Chapter 1

Introduction

1-1 Background

Because of climate change, the growing demand for fresh water becomes an essential problem for The Netherlands and other European countries due to the rising sea level and more frequent droughts. Salt intrusion through sea locks can have negative effects on the required salinity of the fresh inland water for ecological reasons, agricultural use, and drinking water standard [10]. When opening the lock gate during ship traffic, a gravity current occurs between the fresh and salt water. Differences in the hydrostatic pressure causes an induced flow of salt water along the bottom of the river and an opposite seaward flow of fresh water on top, as presented in Fig.1-1 [11].

The salt intrusion process causes mixing of fresh and salt water, which may occur gradually over tens of kilometers. Therefore, the increase in ship traffic intensity, as well as the construction of new locks, calls for proper mitigating measures. One of the available mitigating measures is the application of bubble screens at the locks between fresh and salt water, as presented in Fig.1-2. A screen of air bubbles is generated by injecting compressed air into the bottom of the lock, and this acts as a pneumatic barrier. Theoretical prediction on the

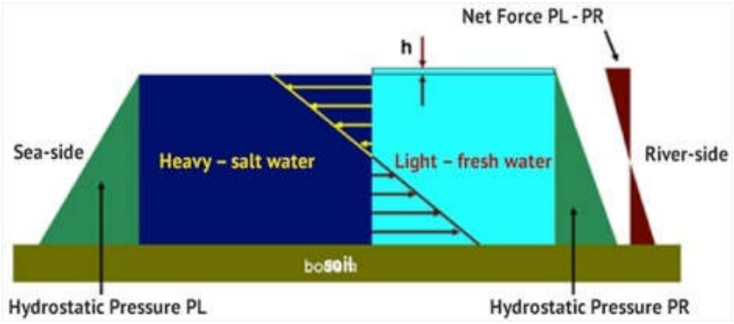

Figure 1-1: Schematic view of salt intrusion between sea and river [1].

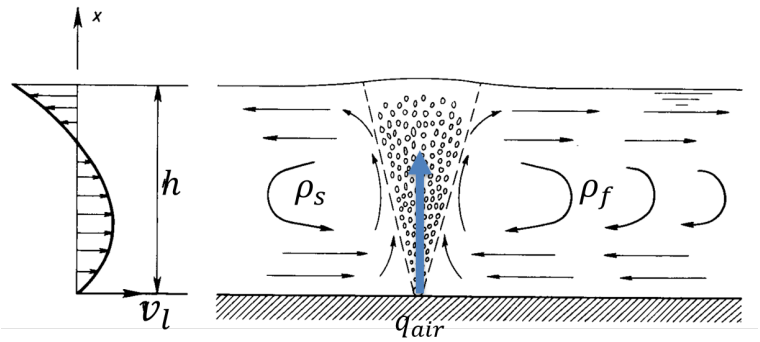

Figure 1-2: Schematic view of bubble screen and horizontal current velocity [2].

performance of the bubble screen has been carried out by Abraham and Van der Burgh early in the 1960s based on the experiments in the Kornwerderzand and IJmuiden locks [2, 12]. However, it also points out that, while the salt intrusion is reduced by using a bubble screen, the mixing of water from both sides also increases near the surface where the bubbles get dispersed.

Nowadays, more field studies and laboratory experiments have been conducted to investigate the performance of the bubble screen properly. Numerical simulations with the application of Computational Fluid Dynamics (CFD) are also helpful to get insight into the flow in and around the sea locks without requiring costly measurement campaigns. However, current numerical simulations on bubble screens to mitigate salt intrusion are relatively scarce, and the validation of such models has not yet been thoroughly checked. Therefore, an accurate and reliable CFD model for predicting the salt intrusion in the presence of a bubble screen is highly desired.

1-2 Literature Review

During the past decades, quite a few full-scale studies on salt intrusion in the presence of a bubble screen has been performed. Multiple experiments have been conducted by Abraham and Van der Burgh as well as Bulson with a focus on the salt concentration and the velocity distribution in the water, respectively [2, 12, 13]. Theoretical predictions are also derived in both cases by considering the energy and momentum balance. Further, Keetels et al. and Uittenbogaard et al. present an innovative design with a combination of bubble and water screens at the Krammer recreational lock and Stevin lock [14, 15, 16]. A similar test of a bubble screen is also done by Weiler et al. considering the lock operation and the flushing discharge in addition [17].

In recent years, laboratory-scale measurements have also been performed on the bubble screen with the advantage of better control on the boundary conditions. Wen and Torrest have conducted some measurements on the line source bubble plumes for the study of aeration-induced circulation in lakes and reservoirs [18]. Later, Riess and Fanneløp have done similar experiments with a focus on surface currents and recirculation flow [19]. A relatively large scale experiment has been done by Van der Ven and Wieleman, which shows a good agreement with the work done by Riess and Fanneløp [20]. Based on the above experiments, lab-scale

investigations on bubble screens for the study of mitigating salt intrusion were also carried out. In preparation for the full-scale tests, Keetels et al. have performed tests on a bubble screen in a flume consisting of two compartments with salt and fresh water, respectively [14]. Recently, to assess the difference in the performance of varying bubble screen operation, more accurate measurements are used by Van der Ven and Oldenziel from Deltares, including Particle Image Velocimetry (PIV), conductivity measurements and dye measurements [21]. Two master students from TU Delft, Kurian and Nikolaidou also contributed to the work to gain sufficient data for further validation of CFD modeling, which will be introduced in the following sections [3, 4].

CFD modeling of gas-liquid flows has been widely used recently for reliable predictions of the flow behavior. Quite a lot of modeling has been done on bubble columns and bubble plumes accurately and efficiently, while work on modeling bubble screens or bubble curtains is comparatively lacking. The Euler-Euler and Euler-Lagrange approaches are the most used approaches to simulate two-phase flows. The Euler-Euler approach, also known as the two-fluid model approach, is the preferred method to use when simulating large-scale systems. In this continuum model, only the macroscopic flow field is resolved for both phases, and closures are required for subfilter-scale dispersive stresses and the drag force between two phases. Among the simulations on bubbly flow, Sokolichin et al. pointed out that the pressure force and the drag force are most important in interface forces between a liquid and a gas [22]. However, Dhotre et al. and McClure et al. stated that the lift force, turbulent dispersion force, and bubble-induced turbulence also play an important role [23, 24].

The Euler-Lagrange approach treats the liquid phase as the continuum phase, while the discrete bubble phase is represented by solving Newton's equation of motion per bubble. Bubble-bubble interactions, including coalescence and break-up, are explicitly accounted for, which makes the method computationally very expensive. Studies on bubble plume behavior based on Large-Eddy Simulation (LES) framework by Bruno Fraga et al. have shown good agreement with experiments [25]. An Euler-Lagrange LES model using stochastic modeling of the bubble collisions is further proposed by Kamath et al. [26].

Another approach by coupling the Population Balance Model (PBM) with the two-fluid model is also applied to predict the distribution functions of the bubble motion and the variation of their properties. Askari et al. [27, 28] have shown a comparison of the four solution methods for PBM and showed that the PBM method provides a reasonable prediction for bubble columns.

For simulations of bubble screens in the presence of salt intrusion, Keetels et al. have developed a qualitative 2D Euler-Euler model test for the field study [14]. Meerkerk et al. have conducted a successful 3D Euler-Euler model validation of the bubble screen, but in a pure fresh water without considering the mitigating performance [29]. They also pointed out that the $k-\epsilon$ model may be questionable because of high turbulent viscosity ratios, and the two-dimensional domain cannot reproduce the lab-scale velocity profile.

1-3 Project Goals and Approach

Salt intrusion through ship locks contributes to a negative impact on the salinity of inland water supply, and gradually becomes a big challenge with increasing shipping intensity and

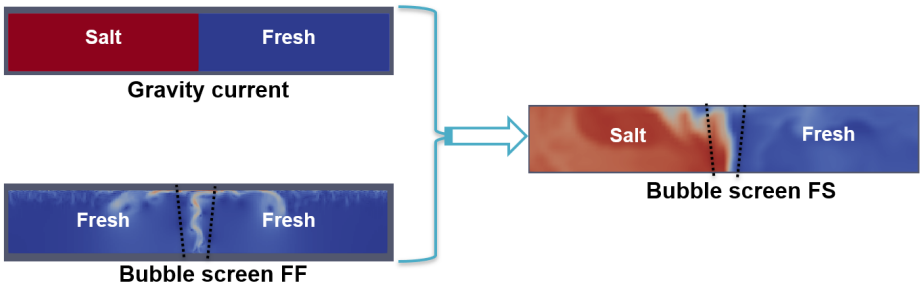

Figure 1-3: Sketch of approach taken in current project.

enormous modern lock sizes. The need exists for a reliable numerical model regarding the costly large-scale equipment, as well as the vast amount of time needed for field measurements. To better predict salt intrusion, the model should be able to correctly describe the flow dynamics of the bubble screen in water with a salinity gradient. Also, different design and operation optimization of a bubble screen should be taken into consideration for optimal performance. Hence, the goal of the present study is three-fold:

1) Use an Euler-Euler CFD model to assess the performance of bubble screen under salt intrusion.

2) Employ a mass transport equation for salt concentration and select an approximate turbulence model for an accurate description of the gravity current and bubble motions.

3) Optimize the relevant parameters of the bubble screens, including Froude air number and the bubble diameter, for better performance in the fresh-salt water systems.

The work is conducted in the framework of a joint TU Delft/Deltares master project, where Deltares is hydraulic institute located in Delft. The intention is to validate the simulation using the commercial CFD package Fluent 17.2 with the lab-scale experiments previously conducted by Deltares. In order to gain a comprehensive understanding in the dynamics of salt intrusion in the presence of a bubble screen, the current project takes the approaches as sketched in Fig.1-3. As illustrated in the picture, a flume is separated into two compartments. Initially, each compartment is filled with fresh water or salt water to generate an either fresh-fresh (FF) or fresh-salt (FS) water system. First, a simulation of a gravity current is conducted both in Fluent 17.2 and OpenFOAM 6 to study the mixing of fresh and salt water in the absence of the bubble screen. The mass transport equation is used here to describe the transport of salt. Different turbulence models are compared for their fresh/salt mixing performance. Then simulation of a bubble screen in the fresh-fresh system is performed in Fluent 17.2 with the Euler-Euler approach to investigate the dynamics of a bubble screen in pure fresh water. Finally, by employing the mass transport equation for the salt concentration in the Euler-Euler model, analysis of the dynamics of the bubble screen for separating fresh and salt water is carried out.

1-4 Thesis Outline

Chapter 2 gives a detailed introduction to the lab-scale experiments done by Deltares, including the experimental setups and measurements, the results of which will be used to validate with the numerical simulations. Chapter 3 presents the gravity current case and describes in detail the mass transport equation for the salt concentration and the turbulence model. Chapter 4 explains the methodology and the solution method to model multiphase flow using an Euler-Euler approach, and the simulation results of the bubble screen in the fresh-fresh water system will be presented and analyzed. Chapter 5 delivers the theory of the bubble screen in mitigating the salt intrusion and conducts the simulations by employing the mass transport equation for the salt concentration to the Euler-Euler model. Chapter 6 gives the overall conclusions and recommendations for future work. Appendix A displays additional results of the above simulations. Appendix B briefly discusses the efforts to perform simulations in OpenFoam by compiling a new solver, which implements an active scalar transport equation into the existing multiphase solver.

Chapter 2

Lab-scale Experiments

In this chapter, the lab-scale experiments previously conducted by Deltares will be described. An overview of the experimental setup is presented, including the geometry and the features of the bubble screen. The same properties will be applied for the simulations in the following chapter. The experimental measurements are briefly introduced, since they will be the major source for further validation.

2-1 Introduction

Plenty of lab-scale experiments on bubble screens have been performed at Deltares. Detailed particle image velocimetry (PIV) measurements have been performed on the fresh-fresh water system for the recording of the flow velocities. Conductivity measurements are used to measure the mixing of water from both sides of the bubble screen, while dye coloring measurements make the mixing visible [21]. The bubble size is also recorded and analyzed for the understanding of the exchange mechanism of fresh and salt water through the bubble screen [9]. Post-processing based on these measurements, provided sufficient data for the validation of CFD simulations. The details of the experimented setup will be presented in the following, and the same flow geometry will be considered in the CFD simulations conducted in the present study.

2-2 Experimental Set-up

A plexiglass water tank was used for the experiment with a length, depth, and height of 2.40 m, 0.50 m, and 0.70 m, respectively. A plate was vertically placed in the middle to separate the tank into two compartments alike a sea lock gate. Two rows of bubble generators were located at the bottom of both sides of the plate to generate bubble screen, Depending on the salinity of the water in both compartments before the start of the experiments, experiments conducted can be referred as either a fresh-fresh or a fresh-salt water system. For both cases, the tank

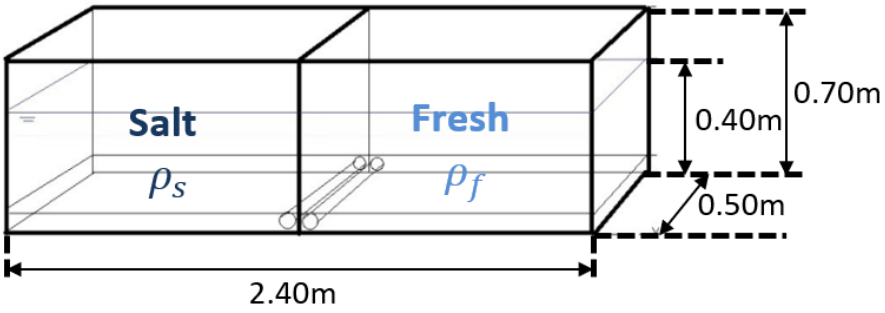

Figure 2-1: Schematic view of the tank geometry [3].

was filled with water at room temperature up to a height of 0.4 m. Two fluids with densities of approximately 1000 kg/m^3 and 1021 kg/m^3 were applied. The geometry of the tank is shown in Fig.2-1.

Two types of bubble spargers were tested to study the effect of the bubble size. One of them was a simple PVC tube with a row of small holes, and the other was a porous air stone, which is normally used in aquariums. The two PVC tubes were located parallel to each other with a distance of 7.5 cm between the tube edges, each with a length of 50 cm and an outer diameter of 4.0 cm. 90 holes with a diameter of 0.8 mm were drilled along each tube to create bubbles with a diameter between 6mm and 8 mm. The bubble output was directed under an angle of approximately 30^o relative to the vertical plane with the two bubble streams flowing towards each other. Pictures of the design are shown in Fig.2-2(a)(b). The four porous stones were placed in the center of the tank as two rows, each with a length of 24.6 cm and a width of 2.5 cm. A distance of 2 cm is set, and the diameter of the bubbles created is around 2 mm. Pictures of the design are shown in Fig.2-2(c)(d).

2-3 Experimental Measurements

In fluid dynamics, the use of scaling laws is an important step in research. The Froude air number is derived by Abraham and Van der Burgh, which is essential for scaling air bubble screens. The Froude air number represents the ratio of kinetic energy from the rising bubbles to the potential energy of the gravity current [2, 12]. For small bubbles in the current project, where the relative velocity of the gas phase to liquid phase can be negligible compared with the velocity of the surrounding water, the expression is shown as follows:

$$Fr_{air} = \frac{(Q_a g)^{\frac{1}{3}}}{(g' H)^{\frac{1}{2}}} \tag{2.1}$$

where Q_a is the flow rate of air per unit time per unit width of the tank at atmospheric pressure. $g' = g\Delta\rho/\rho_{l,s}$ is the rescaled gravitational acceleration. $\Delta\rho$ is the difference in density between the salt water and the fresh water. $\rho_{l,s}$ is the density of salt water. H is the water depth. In Chapter 5, this parameter will be explained more thoroughly.

(a) Snapshot of PVC tubes setup.

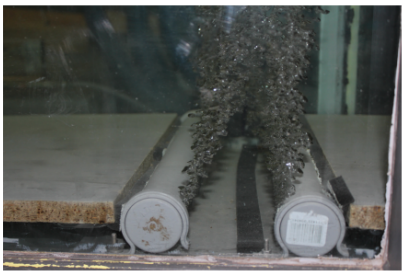

(b) Snapshot of PVC tube bubble screen.

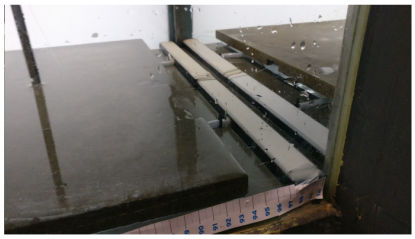

(c) Snapshot of porous stones setup.

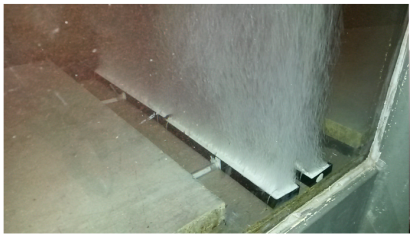

(d) Snapshot of porous stone bubble screen.

Figure 2-2: Pictures of the design of the bubble screen [4].

Table 2-1: Froude air numbers and corresponding air flow rates [3, 4]

Fr_{air}	Flow rate $[NL/min]$	Flow rate $[m^3/s]$
0.80	33.50	$5.58 * 10^{-4}$
0.95	55.96	$9.33 * 10^{-4}$
1.10	86.86	$14.5 * 10^{-4}$

Previous experiments by Deltares have shown that Fr_{air} should be between 0.80 and 1.2 for bubble screens to work properly [30]. Between these values, a balance between the kinetic energy of the rising bubble plume and the potential energy of the gravity current will be achieved, and thus the bubble screen will act more as a barrier instead of a mixer. Multiple Froude air numbers and corresponding airflow rates are investigated for the performance of the bubble screen, as shown in Table 1. The unit of the air flow rate in normal liter per minute is typically used in hydraulic applications, which represents the flow rate in normal conditions, being 1 atmospheric pressure and 0 $^{\circ}C$. The air flow rate in m^3/s is taken from Nikolaidou [4].

2-3-1 PIV Measurements in Fresh-fresh Water System

PIV measurements have been performed only in a fresh-fresh water system to investigate the liquid flow velocities. The flow was calibrated with 100 μm red fluorescent particles that were illuminated by green laser light. A 4M CCD camera was placed at a distance of 1.157 m from the front of the tank. Two pulses are fired with a short delay in between, providing the camera with a double-exposed image of the particles in the flow. The velocities of the flow are hence

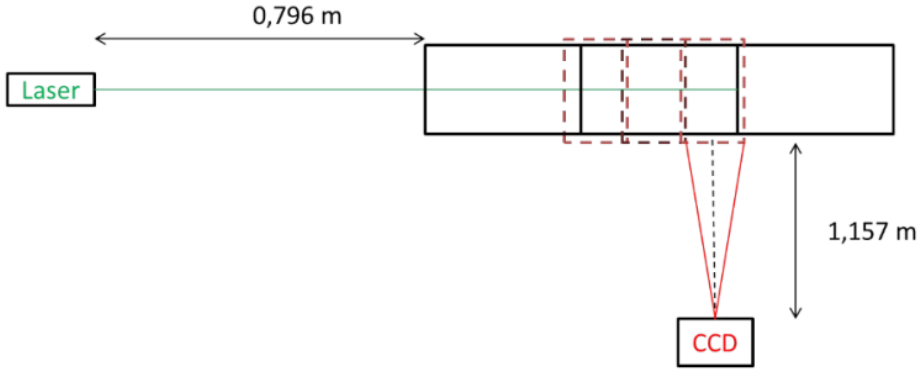

Figure 2-3: Schematic view of the PIV measurements setup [5].

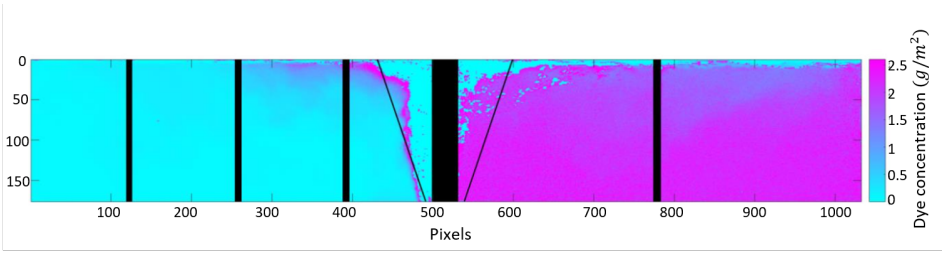

Figure 2-4: Processed image of the dye coloring measurements [3].

proportional to the moving distance of the particles between the pulses. LaVision software DaVis was used for the further post-processing of the acquired image [4]. A schematic view of the PIV setup is presented in Fig.2-3.

2-3-2 Dye Coloring Measurements in Fresh-salt Water System

In order to capture the mixing of fluid in the experiment, an optical dye coloring measurement system has been used for the fresh-salt water system. The salt water was colored with coloring agent Cole-Parmer Blue Tracer Dye Concentrate to visualize the density difference. A LaVision Flowmaster 3S CCD camera was placed at a distance of 11.6 m placed in front of the water tank to track the flow. Measurements lasted for 2 minutes after removing the lock gate. Greyscale images were obtained and converted to concentration fields using a detailed calibration. Fig.2-4 is an example of the processed image, where bubbles, the middle aluminum support, and the conductivity rods are masked as black.

Conductivity Measurements

Four conductivity measurement devices/rods were used to measure the local salinity. On each rod, there are six measuring points/electrodes below the water level. Three devices were set on the fresh water side and one on the salt water side. These measurements were used to validate the images from the dye coloring measurements. A good agreement is shown between the data from the conductivity measurement and the data deduced from image processing. The measuring points are shown in Fig.2-5.

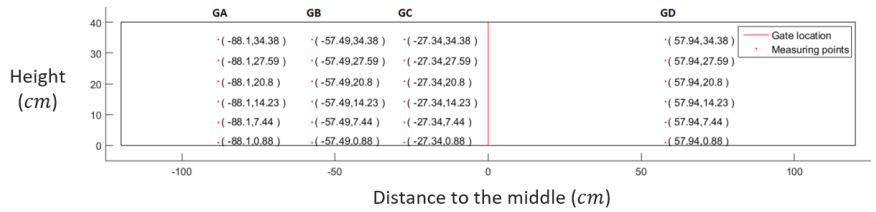

Figure 2-5: Schematic view of the conductivity measurements setup [3].

Table 2-2: Mean sizes of air bubbles corresponding to Froude air numbers generated with PVC tubes [9].

Fr_{air}	Bubble length $[mm]$	Bubble height $[mm]$
0.80	6.6	4.2
0.95	7.8	4.3
1.10	7.9	4.6

2-3-3 Bubble Size Analysis

A brief bubble size analysis has also been performed for the fresh-fresh water system by the photos recorded by the CCD camera. The data is pretty important for numerical simulation input. For the PVC tubes, it could be seen from the analysis that the bubbles looked approximately as ellipsoids with a size varying between 4 mm and 8 mm. The mean sizes of the air bubbles are shown in Table 2-2. However, for the porous stone, bubbles with a diameter between 1 mm and 2 mm have been observed, but a detailed analysis was not conducted. It is worth noting that the ions in the salt water usually increase the surface tension and therefore results in a smaller bubble sizes if the concentration of ions is not too low [31]. Unfortunately, this has not been investigated and may need further study.

Chapter 3

Gravity Current In A Fresh-Salt Water System

In this chapter, the simulation of gravity current will be presented. To correctly model the mixing of two miscible flows, the mass transport equation for salt concentration is employed to track the transport of salt as a solute. Furthermore, the density of the liquid as a solution can be expressed by the concentration of species. Thus, the purpose of this chapter is to validate the application of the mass transport equation and the concentration-density relation with relevant experimental results described in Chapter 2. An introduction to the basic theory and currently used turbulence model will be shown first. Then, simulation results for a gravity current will be analyzed, and some conclusions and remarks will be given regarding the mass transport involved and the turbulence model used.

3-1 Introduction

Gravity currents form when a heavier fluid propagates into a lighter one in a predominantly horizontal direction. Significant efforts have been undertaken to study the gravity currents produced by lock exchange as a classic experiment. A hydraulic theory is developed by Benjamin to describe the front speed and the height of gravity current based on mass and momentum conservation, and from this a Froude number of 0.5 is expected [32]. Here the Froude number for gravity current is different from the bubble screens, which is a ratio of inertial forces relative to the gravitational forces:

$$Fr_g = \frac{U}{\sqrt{g'H}} \tag{3.1}$$

where $g' = g * (\rho_1 - \rho_2)/\rho_1$ is the rescaled gravitational acceleration, U is the front velocity of the salt tongue and H is the water depth.Benjamin's theory also suggested that the energy dissipation due to turbulence and mixing could strongly influence the flow dynamics. Yih also derived an expression for the velocity of gravity currents for the simple case of two fluids

in a finite box separated by a barrier, and same Froude air number as Benjamin's theory is predicted [32]. In the experiments with this setup, Yih found the salt tongue head velocity is about 0.46-0.47 $\sqrt{g'H}$. An alternative theoretical treatment by Shin et al. based on energy conservation shows that the Froude number for a gravity current with a rigid top domain is in a range of 0.42-0.46 [11]. Further simulations in both 2D and 3D done by Cantero et al. suggest an even lower Froude number [33].

3-2 Numerical Model

3-2-1 Governing equations

Since current case is considered as the fresh-salt water system in the absence of a bubble screen, the governing equations for a variable-density fluid are the incompressible Navier-Stokes equations. The conservation equations for mass and momentum are as follows:

$$\frac{\partial \rho_l}{\partial t} + \nabla \cdot (\rho_l \mathbf{u}) = 0 \tag{3.2}$$

$$\frac{\partial \rho_l \mathbf{u}}{\partial t} + \nabla \cdot (\rho_l \mathbf{u}\mathbf{u}) = -\nabla P + \nabla \cdot \boldsymbol{\tau} + \rho_l \mathbf{g} \tag{3.3}$$

where P is the static pressure, and $\mathbf{g}$ is the gravitational acceleration. The stress tensor $\boldsymbol{\tau}$ is given by

$$\boldsymbol{\tau} = \mu_{l,eff}[\nabla \mathbf{u} + (\nabla \mathbf{u})^T - \frac{2}{3}(\nabla \cdot \mathbf{u})\mathbf{I}] \tag{3.4}$$

where $\mu_{l,eff}$ is the effective dynamic viscosity and $\mathbf{I}$ is the unit tensor.

Mass Transport Equation

To correctly model the gravity current produced by the lock exchange, the transport of the salt between the fresh and salt water needs to be described by a mass transport equation apart from the macroscopic mass and momentum conservation for the liquid. The transport of species is expressed by the convection-diffusion equation for the concentration of the salt water c:

$$\frac{\partial c}{\partial t} + \nabla \cdot (c\mathbf{u}) - \nabla \cdot (D \nabla c) = 0 \tag{3.5}$$

where the first term represents the transient transport of the mass, the second term represents the convection of mass caused by the flow, and the last part model the diffusion flux due to concentration gradients using Fick's law [34]. D in the last term represents the molecular diffusivity in m^2/s.

Concentration-density Relation

In reality, the density of sea water mainly depends on the temperature, pressure, and salt concentration. In this case, at constant ambient temperature and pressure, density has an

approximately linear relationship with the salinity [35]. Therefore, the density of the liquid can be coupled with the concentration of the salt water as:

$$\rho_l = (1-c)\rho_f + c\rho_s \tag{3.6}$$

where the subscripts f, s denote the fresh water and salt water, respectively. It is remarked that the density difference between fresh water ($\rho_f = 998.21\ kg/m^3$) and salt water ($\rho_s = 1020\ kg/m^3$) is relatively small. It is therefore assumed that salt concentration only has an influence on the liquid mass density, and that the influence on dynamic viscosity and molecular diffusivity can be neglected.

3-2-2 Turbulence Model

A large variety of turbulence models for simulating turbulent flows, including the two-equation $k-\epsilon$ model, the shear-stress transport (SST) $k-\omega$ model, and the LES model have been well tested on the modeling of gravity current[36, 37, 38, 39]. The standard $k-\epsilon$ model, the SST $k-\omega$ model, and the LES model are considered here. The former two, based on the Reynolds-averaged Navier-Stokes (RANS) equations, are able to catch the main characteristics of the flow with a low computational effort, while the LES model reduces the errors by directly capturing the large-scale motions and modelling only subgrid-scale turbulent motions.

Favre-averaged Equations

For density-varing flows, The RANS equation can be interpreted as Favre-averaged Navier-Stokes equations. As such, the continuity and momentum equation can be applied on flows with variable densities as follows:

$$\frac{\partial \overline{\rho_l}}{\partial t} + \nabla \cdot (\overline{\rho_l}\widetilde{\mathbf{u}}) = 0 \tag{3.7}$$

$$\frac{\partial \overline{\rho_l}\widetilde{\mathbf{u}}}{\partial t} + \nabla \cdot (\overline{\rho_l}\widetilde{\mathbf{u}}\widetilde{\mathbf{u}}) = -\nabla \overline{P} + \nabla \cdot \widetilde{\boldsymbol{\tau}} - \nabla \cdot (\overline{\rho_l \mathbf{u}'\mathbf{u}'}) \tag{3.8}$$

where $\widetilde{\mathbf{u}} = \frac{\overline{\rho_l \mathbf{u}}}{\overline{\rho_l}}$ is the Favre-averaged mean velocity of the flow, $\overline{P}$ is the mean pressure, and $\mathbf{u}' = \mathbf{u} - \widetilde{\mathbf{u}}$ is the Favre-averaged fluctuating velocity. The mean stress tensor $\widetilde{\boldsymbol{\tau}}$ is defined as

$$\widetilde{\boldsymbol{\tau}} = \mu_l[(\nabla\widetilde{\mathbf{u}} + (\nabla\widetilde{\mathbf{u}})^T) - \frac{2}{3}(\nabla \cdot \widetilde{\mathbf{u}})\mathbf{I}] \tag{3.9}$$

Also, a Favre-averaged form of the mass transport equation can be obtained as:

$$\frac{\partial \overline{c}}{\partial t} + \nabla \cdot (\overline{c}\overline{\mathbf{u}}) - \nabla \cdot ((D + D_t)\nabla \overline{c}) = 0 \tag{3.10}$$

with $\overline{c'\mathbf{u}'} = -D_t \nabla \overline{c}$ based on a gradient-diffusion hypothesis. D_t here refers to the turbulent diffusivity derived as:

$$D_t = \frac{\nu_{l,t}}{Sc_t} \tag{3.11}$$

where $\nu_{l,t}$ represents the turbulent kinematic viscosity of the liquid, and Sc_t represents the turbulent Schmidt number. The turbulent Schmidt number Sc_t is normally treated as a

constant. Chung et al. and Tominaga et al. have tested different values of the turbulent Schmidt number for the effect on the prediction of the flow and concentration distribution [40, 41]. A minimal effect is found on the prediction of the velocity, while a small impact is found on the concentration profiles. Here for the gravity current, the value is set to 0.7 based on previous research by Pelmard et al. [42].

Standard $k-\epsilon$ Model

The additional terms $-\overline{\rho_l \mathbf{u}'\mathbf{u}'}$ appeared in Eq.(3.8) is called the Reynolds stress component. The Boussinesq hypothesis is employed to model the Reynolds stress with the mean velocity gradients,

$$-\overline{\rho_l \mathbf{u}'\mathbf{u}'} \approx \mu_{l,t}(\nabla\widetilde{\mathbf{u}} + (\nabla\widetilde{\mathbf{u}})^T) - \frac{2}{3}(\overline{\rho_l}k + \mu_{l,t}(\nabla \cdot \widetilde{\mathbf{u}}))\mathbf{I} \tag{3.12}$$

where k is the turbulent kinetic energy. The turbulent dynamic viscosity $\mu_{l,t}$ is calculated with

$$\mu_{l,t} = \overline{\rho_l} C_\mu \frac{k^2}{\epsilon} \tag{3.13}$$

Here C_μ is a constant equal to 0.09 and ϵ is the dissipation rate. The turbulent kinetic energy k and its dissipation rate ϵ are obtained from the following transport equations:

$$\frac{\partial \overline{\rho_l} k}{\partial t} + \nabla \cdot (\overline{\rho_l} k \widetilde{\mathbf{u}}) = \nabla \cdot [(\mu_l + \frac{\mu_{l,t}}{\sigma_k})\nabla k] + G_k + G_b - \rho_l \epsilon \tag{3.14}$$

$$\frac{\partial \overline{\rho_l} \epsilon}{\partial t} + \nabla \cdot (\overline{\rho_l} \epsilon \widetilde{\mathbf{u}}) = \nabla \cdot [(\mu_l + \frac{\mu_{l,t}}{\sigma_\epsilon})\nabla \epsilon] + C_{1\epsilon}\frac{\epsilon}{k}(G_k + C_{3\epsilon}G_b) - C_{2\epsilon}\overline{\rho_l}\frac{\epsilon^2}{k} \tag{3.15}$$

where standard values are used for the constants: $C_{1\epsilon} = 1.44, C_{2\epsilon} = 1.92, \sigma_k = 1.0, \sigma_\epsilon = 1.3$. G_k represents the generation of turbulence kinetic energy due to the mean velocity gradients:

$$G_k = -\overline{\rho_l \mathbf{u}'\mathbf{u}'}\frac{\partial u_j}{\partial x_i} \tag{3.16}$$

G_b is the generation of turbulent kinetic energy due to buoyancy.

Buoyancy-corrected $k-\epsilon$ Model

To model the buoyancy terms, the simple gradient diffusion hypothesis (SGDH) is applied here:

$$G_b = -\frac{\mu_{l,t}}{\rho_l \sigma_t}\nabla(\overline{\rho_l}) \cdot g \tag{3.17}$$

with σ_t as the turbulent Prandtl number. While the buoyancy effects on the generation of k are always included, the degree to ϵ is affected by the constant $C_{3\epsilon}$. Normally this constant is set to 0 without considering the buoyancy effects on ϵ. A corrected model is considered by using the expression shown as:

$$C_{3\epsilon} = tanh\left|\frac{V}{U}\right| \tag{3.18}$$

where V is the component of the mean flow velocity parallel to the gravitational vector, and U is the component of the flow velocity perpendicular to the gravitational vector. A significant

number of other buoyancy modifications are tested by using methods such as the generalized gradient-diffusion hypothesis (GGDH) and adjusting the relative $C_{3\epsilon}$ constant, as shown by Chung et al. and Bahari et al. [41, 43]. They also point out that the predictions are very sensitive to the choice of $C_{3\epsilon}$. A similar conclusion is also given by Brescianini et al. that the most suitable buoyancy model is dependent of the kind of the experiment conducted [44].

$k-\omega$ SST Model

$k-\omega$ SST model is developed by Menter combining the $k-\omega$ model in the near-wall region and the $k-\epsilon$ model in the far field [45]. The turbulent kinetic energy k and the specific dissipation rate ω are obtained from the following transport equations:

$$\frac{\partial \overline{\rho_l} k}{\partial t} + \nabla \cdot (\overline{\rho_l} k \widetilde{\mathbf{u}}) = \nabla \cdot [(\mu_l + \frac{\mu_{l,t}}{\sigma_k}) \nabla k] + G_k - Y_k \tag{3.19}$$

$$\frac{\partial \overline{\rho_l} \omega}{\partial t} + \nabla \cdot (\overline{\rho_l} \omega \widetilde{\mathbf{u}}) = \nabla \cdot [(\mu_l + \frac{\mu_{l,t}}{\sigma_\omega}) \nabla \omega] + G_\omega - Y_\omega + D_\omega \tag{3.20}$$

G_k, same as Eq.(3.16), represents the generation of k, and $G_\omega = \frac{\alpha_\infty}{\nu_{l,t}} G_k$ represents the generation of ω. $Y_k = \overline{\rho_l} \beta^* k \omega$ and $Y_\omega = \overline{\rho_l} \beta \omega^2$ represent the dissipation of k and ω due to turbulence. $\sigma_k = (F_1/\sigma_{k,1} + (1-F_1)/\sigma_{k,2})^{-1}$ and $\sigma_\omega = (F_1/\sigma_{\omega,1} + (1-F_1)/\sigma_{\omega,2})^{-1}$ are the turbulent Prandtl numbers for k and ω. D_ω represents the cross-diffusion term as:

$$D_\omega = 2\,(1-F_1)\,\rho_l \sigma_{\omega,2} \frac{1}{\omega} \frac{\partial k}{\partial x_j} \frac{\partial \omega}{\partial x_j} \tag{3.21}$$

The turbulent dynamic viscosity is calculated as:

$$\mu_{l,t} = \frac{\rho k}{\omega} \frac{1}{\max\left[\frac{1}{\alpha^*}, \frac{SF_2}{a_1 \omega}\right]} \tag{3.22}$$

where S is the strain rate magnitude, F_1 and F_2 are the blending functions which ensures a smooth transition between the $k-\omega$ model and the $k-\epsilon$ model, and α^* is determined based on a low-Reynolds-number correction. Other model constants are given by $\alpha_\infty = F_1 \alpha_{\infty,1} + (1-F_1)\alpha_{\infty,2}$, $\alpha_{\infty,1} = -0.287$, $\alpha_{\infty,2} = 0.266$, $\beta = F_1 \beta_1 + (1-F_1)\beta_2$, $\beta^* = 0.09$, $\beta_1 = 0.075$, $\sigma_{k,1} = 1.176$, $\sigma_{\omega,1} = 2.0$, $\sigma_{k,2} = 1.0$, $\sigma_{\omega,2} = 1.168$, $\beta_2 = 0.0828$, $\kappa = 0.41$, $\alpha_1 = 0.31$.

LES Model

Large-Eddy Simulation (LES) is chosen for simulating the large-scale dynamics and macroscopic turbulent scales, whereas a subgrid model is used for the smaller scales. The technique has been introduced by Smagorinsky for weather predictions [46]. A box filter kernel is used to cut off the values of the function beyond a half filter width away:

$$G(x) = \frac{1}{\Delta} H_{ea}(\frac{1}{2}\Delta - |x|) \tag{3.23}$$

where Δ is the filter width, x is the physical space, and H_{ea} represents the Heaviside step function. This sub-grid scale (SGS) model describes turbulence in the scales that are smaller

than the filter length Δ. In order to determine the turbulent stresses generated by these motions, turbulent viscosity can be modeled with the Smagorinsky model as:

$$\mu_{l,t} = \rho_l c_s \Delta^2 \sqrt{2\mathbf{S}_{ij}\mathbf{S}_{ij}} \tag{3.24}$$

where c_s is the Smagorinsky constant set as 0.2, and $\mathbf{S}_{ij}$ is the strain rate tensor of the resolved flow. Thus, the effective dynamic viscosity in Eq.(3.4) can be calculated as:

$$\mu_{l,eff} = \mu_l + \mu_{l,t} \tag{3.25}$$

Desjardin et al. point out that the prediction of the LES model is very sensitive to the Smagorinsky constant and the grid size [47]. The best agreement is achieved with the finest grid size but will require more computational resources.

Wall Functions

Wall functions are used to avoid resolving all scales in a turbulent boundary layer. The wall functions use the law of the wall to locally estimate the wall shear stress from the near-wall velocity. By using dimensional analysis, flow behavior can be expressed by means of dimensionless groups $u+$ and $y+$:

$$u+ = \frac{\overline{u}}{u_w} \tag{3.26}$$

$$y+ = \frac{y u_w}{\nu_l} \tag{3.27}$$

$$u_w = \sqrt{\frac{\tau_w}{\rho_l}} \tag{3.28}$$

The near-wall region, depending on the distance y, fluid density ρ_l, kinematic viscosity ν_t, and the wall shear stress τ_w, can be subdivided into three sublayers. The layer where viscosity dominates is called the viscous sub-layer with $y+ \leq 5$. In this layer, linear relationship can be given between the velocity and distance to the wall as:

$$u+ = y+ \tag{3.29}$$

The layer where turbulence dominates is called the log-law region with $30 < y+ < 0.3\delta$. δ here refers to the boundary layer thickness. The velocity and distance to the wall have a logarithmic relationship as:

$$u+ = \frac{1}{\kappa} ln(y+) + B \tag{3.30}$$

where κ is the von Kármán constant generally taken as 0.41, and the constant B equals 5.2. The buffer layer lies between the above two layers, where the effects of viscosity and turbulence are equally important. These sublayers, together with the relationship between $u+$ and $y+$, are demonstrated in Fig.3-1. The enhanced wall treatment is a near-wall modeling method that possesses the accuracy of the standard two-layer approach for fine near-wall meshes and, at the same time, will not significantly reduce accuracy for wall-function meshes.

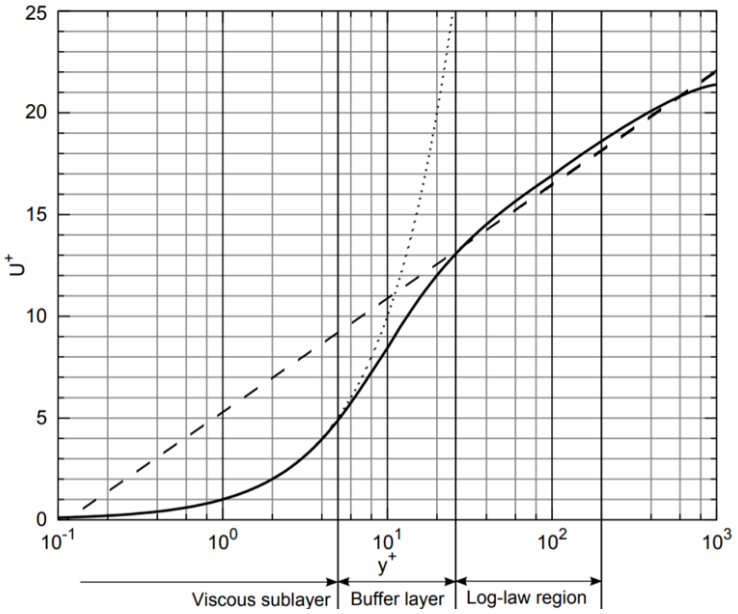

Figure 3-1: Subdivisions of the near-wall region with dotted line: $u+ = y+$, dashed line: $u+ = \frac{1}{\kappa}ln(y+) + B$, and solid line: experimental data [6].

Table 3-1: Relevant physical properties of the gravity current simulations

Parameter	Value	Unit
Ambient Pressure P	101325	Pa
Ambient Temperature T	20.0	$°C$
Fresh water density ρ_f	998.21	kg/m^3
Salt water density ρ_s	1019.21	kg/m^3
Gravity acceleration g	9.81	m/s^2
Liquid dynamic viscosity μ_l	$1.003 * 10^{-3}$	$kg/(m * s)$
Salt diffusivity D	$1.6 * 10^{-11}$	m^2/s

3-3 Simulation Setup

The previously described models are tested with the CFD package Fluent 17.2 for their performance in simulating gravity current in a fresh-salt water system in the absence of a bubble screen. The simulation is conducted with a 3D domain with the same dimension as the lab-scale experiments, as described in Chapter 2. The mixing of the water can be compared with the processed images and data derived from the dye measurements. The relevant physical properties are listed in Table 3-1, with the flow considered as incompressible and isothermal. The density of the fresh water is estimated to be 998.21 kg/m^3 [48]. A density of 1019.21 kg/m^3 is chosen for the salt water to keep the density difference equivalent to the experimental setup. The salt diffusivity is chosen based on research from Poisson et al. on seawater ion diffusivities [49].

The numerical setup is shown in Table 3-2. A mesh grid size of 10 mm is applied in order to have a uniform cubic grid cell. A Courant number is targeted to be below 1 for numerical

Table 3-2: Numerical setting of the gravity current simulations

Parameter	Value
Domain size $[L_x \times L_y \times L_z]$	$2.4\ m \times 0.4\ m \times 0.5\ m$
Grid cells	$240 \times 40 \times 50$
Time step	$0.01\ s$
Full simulation time	$125\ s$

stability with a time step of 0.01 s. Full simulation time is set as 125 s, corresponding to the experiments. The boundary condition for the top is set as a free surface, whereas for the other walls no-slip boundary conditions are applied. The salt water is patched for the right half of the domain with an initial concentration c of 1. Three turbulence models, including the LES, the standard $k-\epsilon$, and the $k-\omega$ SST turbulence model, are used for comparison. The PIMPLE algorithm is used for the pressure-velocity coupling running with OpenFOAM 6, while the coupled algorithm is applied by solving the momentum and pressure-based continuity equations together in Fluent 17.2. The same results are obtained with both methods. Another case of the buoyancy-corrected $k-\epsilon$ model based on the SGDH expression is also simulated with Fluent 17.2.

3-4 Results

Screenshots of the concentration profiles of the "laminar" model at several instances in time are shown in Fig.3-2, together with the dye coloring processed images for comparison. The "laminar" model here means no turbulence model is used, hence the turbulent structures in the flow are partially resolved in a relatively small size grid. A slice in the middle of the domain is selected here. The density profiles for other turbulence models are included in Appendix Fig.A-1 A-2.

As can be seen from the density profiles, a gravity current seems to develop correctly, and the movement of the salt water matches well with the dye coloring images. A more detailed analysis is carried out to obtain the Froude number by measuring the gravity current head displacements at various time steps. It is chosen only to consider the first 9 seconds before the gravity current head reaches the walls at $t = 10\ s$. Linear regression is performed on the data, as shown in Fig.3-3. A Froude number equal to 0.46 is acquired. This result corresponds well with Yih's experiment and the theory by Shin et al. for a rigid top domain. The difference with Benjamin's theory may be caused by the viscosity at the wall, as the theory does not consider energy dissipation.

However, the images of the standard $k-\epsilon$ and the $k-\omega$ SST turbulence model are not corresponding to the experimental results after around 50 s. To further study these phenomena, a quantified analysis is performed on the averaged concentration of salt water c over the left half of the domain as a function of time. The plot is shown in Fig.3-4. The laminar model and LES model agree nicely with the experiment, but the other two models seem to mix the two fluids too quickly. The reason for this may be mainly due to the buoyancy terms presented in the Eq.(3.14-15) and Eq.(3.19-20), since it is not able to correctly account for the buoyancy effects on the production and destruction of turbulent kinetic energy. The buoyancy-corrected

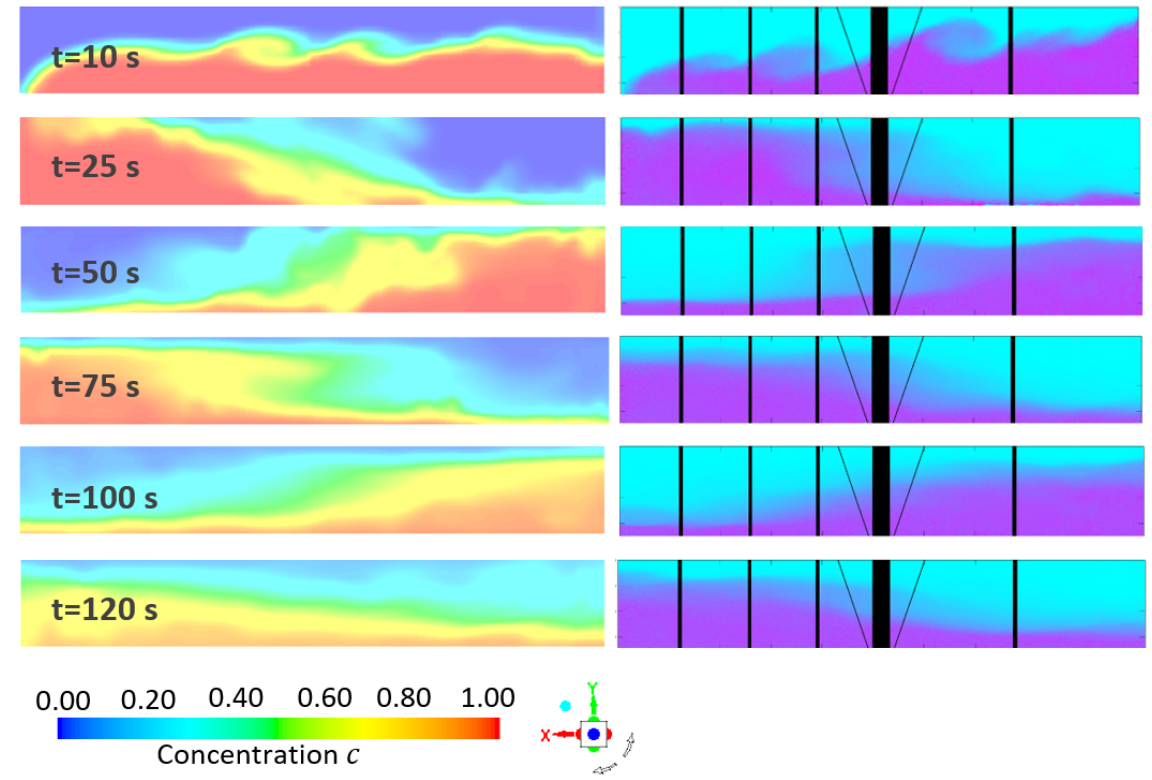

Figure 3-2: Density profiles of the gravity current simulation with the "laminar" model at the middle of the domain $z = 0.25\ m$ (left) and the dye coloring processed images (right) at several time steps using Fluent 17.2.

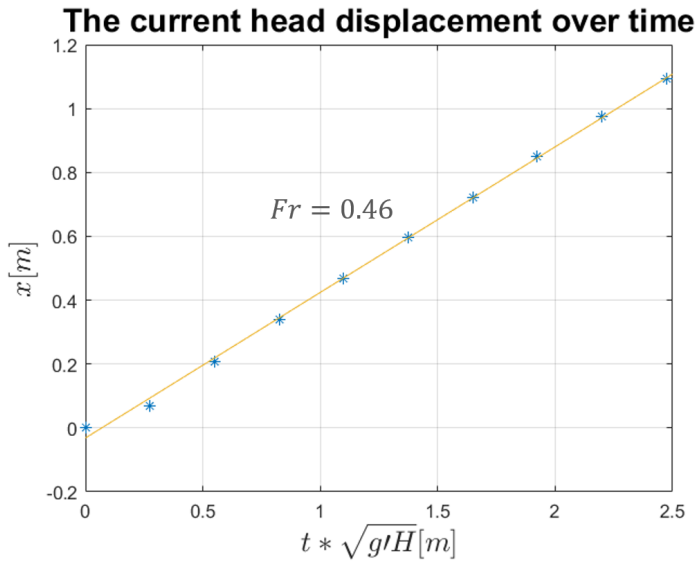

Figure 3-3: Linear regression of the current head displacement over time

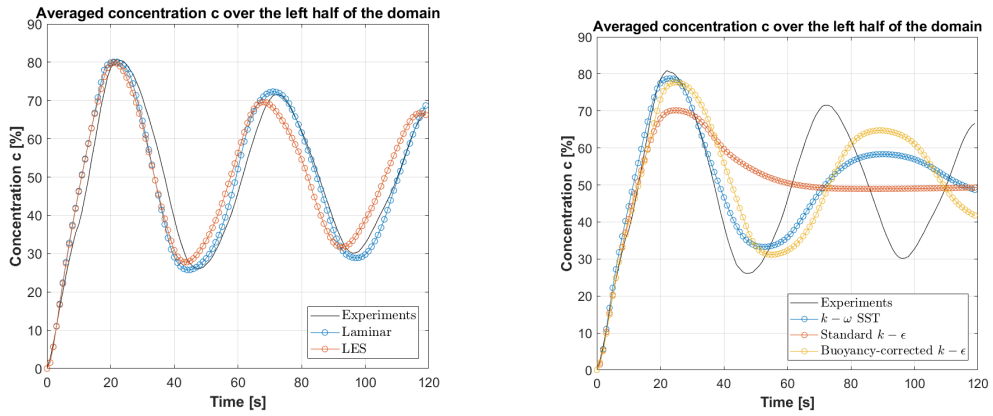

Figure 3-4: Averaged concentration c over the left half of the domain as function of time.

$k-\epsilon$ model indeed shows some improvement but still has a significant deviation compared to experimental data. Tuning the buoyancy constant $C_{3\epsilon}$ or modifying the buoyancy production method may improve the result. However, the results will become unreliable with a different domain size, as $C_{3\epsilon}$ is highly dependent on the flow conditions, which is a severe drawback for the present RANS model.

3-5 Conclusions and Remarks

In this chapter, the implementation of the mass transport equation and the turbulence model are explained for the simulation of gravity current in a fresh-salt water system in an absence of the bubble screen. The results of the simulations are validated with the experimental data and analytical theory from previous work.

The application of the mass transport equation is considered as a success with some assumptions and approximations. Firstly, the density of the liquid is considered as a linear relationship with the salinity at constant temperature and pressure. In reality, the temperature and pressure may change with time. Moreover, the density of the liquid does not depend linearly on the concentration for some species. Secondly, the added salt is considered to have no impact on the salt diffusivities and dynamic viscosity because of the small density difference. However, these terms will vary with different salinity of the liquid. Lastly, the salt diffusivities are taken based on literature values for seawater. This parameter may vary with different seawater conditions.

Regarding the selected turbulence model, it turns out that the gravity current modeled with the LES model has a good agreement with the dye coloring measurements from the experiments, while the standard $k-\epsilon$ and the $k-\omega$ SST turbulence model are less reliable. It is more clear when comparing screenshots of these simulations at the same time step, as shown in Fig.3-5, where turbulent structures like the Kelvin-Helmholtz instability are better captured with the LES model. The LES model resolves the large turbulent flow structures explicitly, while the dissipation scales are modeled. In this way, greater accuracy is provided on the instantaneous resolved flow field, whereas most of this information is lost with the RANS model. Consequently, it is recommended to use the LES model for a more correct

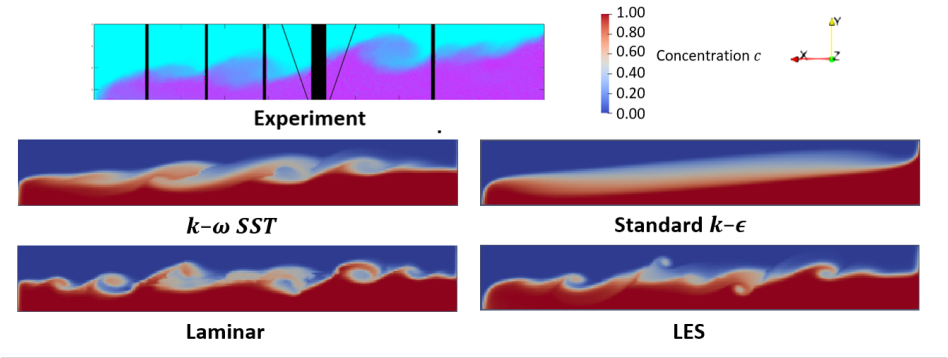

Figure 3-5: Comparison of the density profiles of different turbulence models at $t = 10\ s$ using OpenFOAM 6

simulation of the turbulence structure, as buoyancy effects can not be accurately captured with the RANS models considered here.

In the next chapter, a bubble screen generator will be implemented. Next, simulations will be conducted in the fresh-fresh and fresh-salt water systems, based on the mass transport equation and turbulence model introduced in this chapter. The salt intrusion with the presence of the bubble screen will then be analyzed.

Chapter 4

Bubble Screen In A Fresh-Fresh Water System

4-1 Introduction

Lab-scale experiments on bubble screens in a fresh-fresh water system were previously conducted by Deltares in order to study the flow patterns created by the injection of air bubbles. Field studies at sea locks, together with theory and empirical correlations, also provide useful information on the features of bubble screens. In recent years, more simulations have been performed in the study of bubble plumes as well. To correctly model a bubble screen, accurate treatment of the dispersed phase and the coupling between phases are required. The Euler-Euler approach, which computes the two phases in a Eulerian framework, is considered computationally efficient. In this chapter, the simulation of a bubble screen in a fresh-fresh water system will be presented. The Euler-Euler approach and the solution method will be introduced first. Then the simulation setup, including the grid sizes and the boundary conditions, will be presented. Results will be compared with the PIV data described in Chapter 2 and some empirical correlations. Finally, conclusions and remarks will be summarized about the simulation of a bubble screen using the Euler-Euler approach.

4-2 Numerical Method

4-2-1 The Euler-Euler approach

In the current work, the flow is modeled using the Euler-Euler approach. This model solves for both the gas and the liquid phase in a Eulerian reference frame. The two phases are treated as interpenetrating continua and described by averaged conservation equations. Each cell in the discretized domain contains a certain volume fraction of each phase, and for every phase a set of averaged governing equations are resolved. Thus, the amount of gas in each cell of the mesh is represented by the phase fraction, which results in less computationally

expensive simulations than the so-called discrete phase models in which individual bubbles are tracked [50]. The continuity equation and momentum equation for each phase without interfacial mass transfer are written as:

$$\frac{\partial \alpha_i \rho_i}{\partial t} + \nabla \cdot (\alpha_i \rho_i \mathbf{u}_i) = 0 \tag{4.1}$$

$$\frac{\partial \alpha_i \rho_i \mathbf{u}_i}{\partial t} + \nabla \cdot (\alpha_i \rho_i \mathbf{u}_i \mathbf{u}_i) = -\alpha_i \nabla P + \nabla \cdot \boldsymbol{\tau}_i + \alpha_i \rho_i \mathbf{g} + \mathbf{F}_{I,i} \tag{4.2}$$

where $\rho_i, \alpha_i, \mathbf{u}_i$ are the density, phase fraction, and velocity for phase i. The subscript i can be substituted by l or g, depending on whether the target phase is liquid or gas. The stress tensor for phase i is given by:

$$\boldsymbol{\tau}_i = \alpha_i \mu_i [\nabla \mathbf{u}_i + (\nabla \mathbf{u}_i)^T - \frac{2}{3}(\nabla \cdot \mathbf{u}_i)\mathbf{I}] \tag{4.3}$$

For the momentum equation, the first term at the left-hand side represents the rate of change of momentum. The second term describes the convective flux of momentum. The terms on the right are the pressure gradient, total stress within the phase, body force due to gravity, and the interface interaction force acting on phase i. Two additional equations are required for the phase fraction and the interphase force as:

$$\Sigma \alpha_i = 1 \tag{4.4}$$

$$\Sigma \mathbf{F}_{I,i} = 0 \tag{4.5}$$

These equations state that, due to the global conservation of mass and momentum, the total volume fraction should equal to one, while the total momentum transfer between phases equals zero.

Interphase Interaction Force

The interphase interaction force $\mathbf{F}_{I,i}$ is the most important feature of multiphase flow. This term describes the interaction force between the phases, including the drag force, lift force, virtual mass force, and turbulent dispersion force:

$$\mathbf{F}_{I,l} = -\mathbf{F}_{I,g} = \mathbf{F}_D + \mathbf{F}_L + \mathbf{F}_{VM} + \mathbf{F}_{TD} \tag{4.6}$$

The drag term is the dominant contribution in the interaction force term. The origin of the drag force is due to the resistance experienced by a body moving in a fluid continuum, and can be formulated as follows:

$$\mathbf{F}_D = \frac{3}{4} \rho_l \alpha_g C_D \frac{|\mathbf{u}_g - \mathbf{u}_l|(\mathbf{u}_g - \mathbf{u}_l)}{d_b} \tag{4.7}$$

where d_b is the bubble diameter. The drag coefficient C_D is given by the Schiller and Naumann model [51]:

$$C_D = \begin{cases} 24(1 + 0.15\ \mathrm{Re}^{0.687})/\mathrm{Re} & \mathrm{Re} \leq 1000 \\ 0.44 & \mathrm{Re} > 1000 \end{cases} \tag{4.8}$$

Re is the relative Reynolds number obtained from:

$$\mathrm{Re} = \frac{\rho_l \left|\mathbf{u}_l - \mathbf{u}_g\right| d_b}{\mu_l} \tag{4.9}$$

Tomiyama's model is proposed by Simcik et al. as it is well suited to gas-liquid flows in which the bubbles can have a range of shapes [52, 53]. For high Eötvös numbers, the capped bubbles generate more drag force than spherical or elliptical bubbles. Dhotre et al. derive the coefficient based on Ishii and Zuber model for boiling flow [23]. However, the Schiller and Naumann model is adopted here since it is generally acceptable for all fluid-fluid pairs of phases.

Bubble moving in liquid experiences a lift force due to vorticity upstream to it. The lift force is defined as:

$$\mathbf{F}_L = -\rho_l \alpha_g C_L (\mathbf{u}_g - \mathbf{u}_l) \times (\nabla \times \mathbf{u}_l) \tag{4.10}$$

where C_L is the lift coefficient. In most cases, the lift force is insignificant compared to the drag force. It is only of interest in cases with strong cross flows and hence is neglected here [29].

The virtual mass force accounts for relative acceleration and the additional work performed by the bubbles in accelerating the liquid surrounding the bubble.:

$$\mathbf{F}_{VM} = C_{VM} \alpha_g \rho_l \left(\frac{D\mathbf{u}_l}{Dt} - \frac{D\mathbf{u}_g}{Dt}\right) \tag{4.11}$$

Typically for a rigid sphere, a value of 0.5 is taken for the virtual mass coefficient C_{VM}.

The turbulent dispersion force accounts for the random influence of the turbulent eddies, formulated with Lopez de Bertodano model [54]:

$$\mathbf{F}_{TD} = -C_{TD} \rho_l k_l \nabla \alpha_g \tag{4.12}$$

where $C_{TD} = 1$ is the turbulent dispersion coefficient, and k_l is the liquid turbulent kinetic energy per unit mass.

4-2-2 Turbulence Model

It has been discussed in Chapter 3 that the LES model is recommended for the simulation of the turbulence structure, as the buoyancy effects can not be accurately captured with the investigated RANS models. However, due to the limitation of Fluent 17.2, the LES model is not supported by the Euler-Euler approach. Hence, a "laminar" model will be mainly considered in the simulation of the bubble screen. The "laminar" model here can be regarded as a coarse-grid Direct Numerical Simulation (DNS) with no explicit turbulence modelling. A relatively higher resolution in the grid size of the "laminar" model may be able to capture the turbulent dissipation in small eddies. An alternative method would be using the LES model with the algebraic slip mixture approach, which is a simplified multiphase model. The mixture model solves the continuity equation and the momentum equation for the mixture, the volume fraction equation for the secondary phases, as well as algebraic expressions for the relative velocities. A degassing boundary condition, explained in the next section, should

be applied with a User Defined Function (UDF). But it seems that it is only investigated by Simcik et al. without a detailed description [52].

Still, the RANS models, including the standard $k-\epsilon$ model, are still used here with reults shown in Appendix A-2-1, to see whether the effects of the buoyancy terms still play an essential role in the presence of the bubble screen. The dispersed turbulence model is selected for modeling turbulence in multiphase flows. The standard $k-\epsilon$ model, including the interphase turbulent momentum transfer, is used to predict the turbulence for the continuous phase. Two source terms in the transport equations for k_l and ϵ_l account for the effect of the dispersed phase turbulence, respectively:

$$\Pi_{k_l} = \frac{K_{gl}}{\alpha_l \rho_l}(k_{gl} - 2k_l + \overline{u}_{gl} * \overline{u}_{dr}) \tag{4.13}$$

$$\Pi_{\epsilon_l} = 1.2\frac{\epsilon_l}{k_l}\Pi_{k_l} \tag{4.14}$$

where K_{gl} is the exchange coefficient, $\overline{u}_{gl}$ is the relative velocity and $\overline{u}_{dr}$ is the drift velocity. The turbulent kinetic energy in the dispersed phase k_g is obtained using Tchen's theory that assumes two time scales. The characteristic particle relaxation time is associated with inertial effects acting on a dispersed phase:

$$\tau_{gl}^F = \alpha_g \rho_g K_{gl}^{-1}(\frac{\rho_g}{\rho_l} + C_{VM}) \tag{4.15}$$

The Lagrangian integral time scale is mainly connected with the crossing-trajectory effect:

$$\tau_{gl}^t = \frac{\tau_l^t}{\sqrt{1 + C_\beta \zeta_\tau^2}} \tag{4.16}$$

with:

$$\tau_l^t = \frac{3}{2}C_\mu \frac{k_l}{\epsilon_l} \tag{4.16}$$

$$C_\beta = 1.8 - 1.35cos^2\theta \tag{4.17}$$

$$\zeta_\tau = \frac{\overline{u}_{gl}}{\sqrt{\frac{2}{3}k_l}} \tag{4.18}$$

where θ is the angle between the mean particle velocity and the mean relative velocity. Simonin et al. suggest that the ratio between these two time scales could be used to predict the turbulent quantities of the dispersed phase [55]:

$$k_g = k_l\left(\frac{b^2 + \eta_{gl}}{1 + \eta_{gl}}\right) \tag{4.19}$$

$$k_{gl} = 2k_l\left(\frac{b + \eta_{gl}}{1 + \eta_{gl}}\right) \tag{4.20}$$

$$b = (1 + C_{VM})(\frac{\rho_g}{\rho_l} + 1) \tag{4.21}$$

$$\eta_{gl} = \frac{\tau_{gl}^t}{\tau_{gl}^F} \tag{4.22}$$

The standard $k-\epsilon$ model results shows a great deviation from the experiments and may overestimate the turbulent viscosity as proposed by Deen et al.[56].

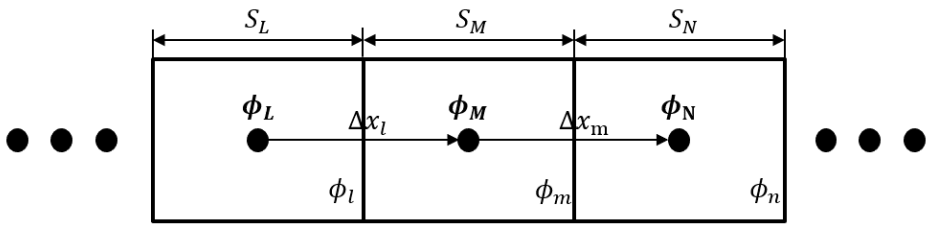

Figure 4-1: A sketch of the one-dimensional control volume around cell M

4-2-3 Solution Method

A control-volume-based technique converts the partial differential equations described above to algebraic equations that can be solved numerically. Consider a transport equation for a scalar quantity ϕ, discretization is applied to each grid cell in the computational domain:

$$\frac{\partial \rho \phi}{\partial t} V_M + \sum_F J_F \phi_F \cdot \mathbf{A}_F = \sum_F D_F \nabla \phi \cdot \mathbf{A}_F \tag{4.23}$$

where V_M is the cell volume, J_F is the mass flux through the face, $\mathbf{A}_F$ is the surface area vector, D_F is the diffusion coefficient for ϕ, ϕ_F is the quantity convected through face F and $\nabla \phi$ is the gradient of ϕ at face F.

Spatial Discretization

For the one-dimensional control volume as sketched in Fig.4-1, discretization on an arbitrary cell M yields:

$$J_m \phi_m - J_l \phi_l = D_F \left(\frac{\phi_N - \phi_M}{\Delta x_n} - \frac{\phi_M - \phi_L}{\Delta x_l} \right) \tag{4.24}$$

where Δx_l and Δx_n are the displacement from the upstream cell centroid to the next cell centroid. Face value ϕ_l and ϕ_n required for the convection terms are interpolated from the cell center value ϕ_L, ϕ_M and ϕ_N using some numerical schemes.

A second-order upwind scheme is applied for the momentum using the following expression:

$$\phi_m = \phi_M + \nabla \phi_l S_M \tag{4.25}$$

$$\nabla \phi_M = \frac{1}{V_M} \sum_F \overline{\phi}_M \cdot \mathbf{A}_F = \frac{1}{S_M + S_L} (\phi_M - \phi_L) \tag{4.26}$$

where the face value $\overline{\phi}_F$ is reconstructed by averaging in two cells adjacent to the face. The volume fraction is computed based on a QUICK scheme. For a uniform grid, the face value is reconstructed by quadratic interpolation in two upwind nodes and one downstream node:

$$\phi_m = \chi \left(\frac{1}{2} \phi_M + \frac{1}{2} \phi_E \right) + (1 - \chi) \left(\frac{3}{2} \phi_M - \frac{1}{2} \phi_L \right) \tag{4.27}$$

with $\chi = 1/8$ yields the traditional QUICK scheme.

Temperal Discretization

For transient simulations, the governing equations are also discretized in time for the first term in Eq.(4.23). A second-order implicit discretization evaluates the spatial discretization $F(\phi)$ at a later time, which is unconditionally stable and can handle large time step:

$$\frac{3\phi^{i+1} - 4\phi^{i} + \phi^{i-1}}{2\Delta t} = F(\phi^{i+1}) \tag{4.28}$$

where Δt refers to a time step, and the superscripts illustrate the specific time.

Pressure-velocity Coupling

The coupled algorithm solves the pressure-based continuity and momentum equations together. Several iterations of the solution loop are performed to obtain a converged solution. The procedures are outlined below:

1) Update the fluid properties based on the current solution.
2) Solve the continuity and momentum equations simultaneously.
3) Solve other transport equations such as turbulence using the previously updated values.
4) Check for convergence of the equation set.

4-3 Simulation Setup

In this section, the simulation setup of a bubble screen in a fresh-fresh water system is presented, including the physical properties and the numerical settings. Details on the boundary conditions and grid size analysis will be carried out.

4-3-1 Physical Properties

The relevant physical properties of the air and water are listed in Table 4-1. The density and dynamic viscosity of both phases are determined based on the ambient pressure and temperature. In the lab-scale experiments, two different spargers are tested with the PVC tube and the porous stone. However, current simulations will only focus on the porous stones, as the simulation results of the bubble screen produced by the PVC sparger are not satisfactory. The performance of the bubble screen generated by the PVC sparger is as poor as that by the porous stone sparger with a quite low Froude air number, as shown in Appendix Fig.A-12. Nikolaidou also meets the same problem in her simulations [4]. The reason may mainly due to that the orifices of the PVC pipes are quite small and hard to mesh. Common treatment by considering the inlet area as a slit of size equal to the bubble diameter does not meet the actual inlet velocity of the PVC sparger. Also, the bubble screen created by the PVC sparger is a relatively dilute plume. The Euler-Euler method may not be able to reproduce the interaction of bubbles in detail. A possible solution would be using a deterministic Euler-Lagrange method, where each individual bubble is tracked throughout the computational domain [57]. The bubble diameter is claimed as 2 mm for the porous stone sparger from the bubble size analysis, while a bubble diameter of 4 mm is also considered for comparison.

Table 4-1: Relevant physical properties of the bubble screen in a fresh-fresh water system simulations

Parameter	Value	Unit
Ambient Pressure P	101325	Pa
Ambient Temperature T	20.0	$°C$
Fresh water density $\rho_{l,f}$	998.21	kg/m^3
Liquid dynamic viscosity μ_l	$1.003 * 10^{-3}$	$kg/(m * s)$
Gas density ρ_g	1.204	kg/m^3
Gas dynamic viscosity μ_g	$1.825 * 10^{-5}$	$kg/(m * s)$
Gravity acceleration g	9.81	m/s^2
Surface tension coefficients γ	$72.86 * 10^{-3}$	N/m
Bubble diameter d_b	2.0	mm

Table 4-2: Numerical setting of the bubble screen in a fresh-fresh water system simulations

Parameter	Value
Domain size $[L_x \times L_y \times L_z]$	$2.4\ m \times 0.4\ m \times 0.5\ m$
Grid cells	$192 \times 32 \times 40$
Time step	$0.05\ s$
Full simulation time	$125\ s$

4-3-2 Numerical Settings

The associated numerical setting is presented in Table 4-2. The geometry of the domain is based on the experimental setup, as listed in Chapter 2. The porous stone spargers are modeled as two slits with a distance of 2 cm in between. For simplification, it is chosen not to include the coalescence and breakup of the bubbles. Also, at the scale of the experiment, the air is considered as an incompressible flow as the influence of pressure difference on air density is a small factor. However, when scaling up to a sea lock size, a compressible liquid method is recommended to be used, which establishes a nonlinear relationship between density and pressure under isothermal conditions. Full simulation time has set to be 125 s, with a time step of 0.05 s to maintain the Courant number below 1.

Grid Resolution

The grid size of the domain is kept constant at 12.5 mm. A coarse mesh with a grid size of 25 mm and a slightly refined mesh with a grid size of 9.5 mm are also taken into consideration for the study of mesh independence. Theoretically, the computational grid needs to be fine enough to resolve the flow structure in all length scale. The smallest length scales are given by the Kolmogorov length scale in a turbulent flow:

$$\eta = (\frac{\nu_l^3}{\epsilon_l})^{\frac{1}{4}} \tag{4.28}$$

Table 4-3: Froude air numbers and corresponding air flow rates for the bubble screen fresh-fresh simulations and experiments

Num. Fr_{air}	Num. flow rate $[L/min]$	Exp. Fr_{air}	Exp. flow rate $[NL/min]$
0.78	33.50	0.80	33.50
0.93	55.96	0.95	55.96
1.08	86.86	1.10	86.86

with ϵ_l represents the average dissipation rate of liquid estimated as:

$$\epsilon_l \sim \frac{u_{l,c}^3}{H} \tag{4.29}$$

where $u_{l,c}$ is the upward liquid velocity caused by the airflow, and H is the height of the domain. Abraham gives the formulation between the upward velocity at the water surface and the air flow rate as [2]:

$$u_{l,c} = 1.2(Q_a g)^{\frac{1}{3}} \tag{4.30}$$

with Q_a as the air flow rate per unit width of the domain. In this way, the ratio of the grid size to the Kolmogorov length scale is in order of approximately $O(10^2)$ for all the air flow rates in Table 4-3, which reveals a lousy resolution in resolving the turbulence fully. The Taylor length scale is also considered here as the grid size of a Kolmogorov length scale would be way beyond the computational capacity. The Taylor length scale is the intermediate length scale below which fluid viscosity significantly affects the dynamics of turbulent eddies in the flow estimated by:

$$\lambda \sim \sqrt{15\nu_l \frac{u_{l,c}^2}{\epsilon_l}} \tag{4.31}$$

The grid size is approximately three times the Taylor length scale of around 5 mm. More precise simulations using a DNS method may need a grid size around that scale.

Boundary Condition

A schematic view of the domain setup is shown in Fig.4.2. The no-slip boundary condition is imposed for the walls of the domain. A fixed velocity is applied for both phases at the inlet area, which is in the place of the porous stone spargers. The different choices of the relevant physical parameters, including the density and the temperature, lead to a minor deviation with the experimental Froude air number. A conversion error of the normal liter in the air flow rates also leads to a Fr_{air} in a fraction smaller than the experiments, as shown in Table 4-3.

The outlet boundary condition for the top surface is imposed as a degassing boundary condition. Generally, this boundary condition handles the outlet as a free surface for the liquid phase, while as a pressure outlet for the gas phase, and thus prevents only the liquid phase from leaving the domain. A negative source term is set to the mass conservation at the cells adjacent to the outlet for removing all the gas phase.

Another option by setting a pressure outlet boundary condition for the top does not work correctly. A comparison of these two boundary conditions is displayed in Fig.4-3. As can be

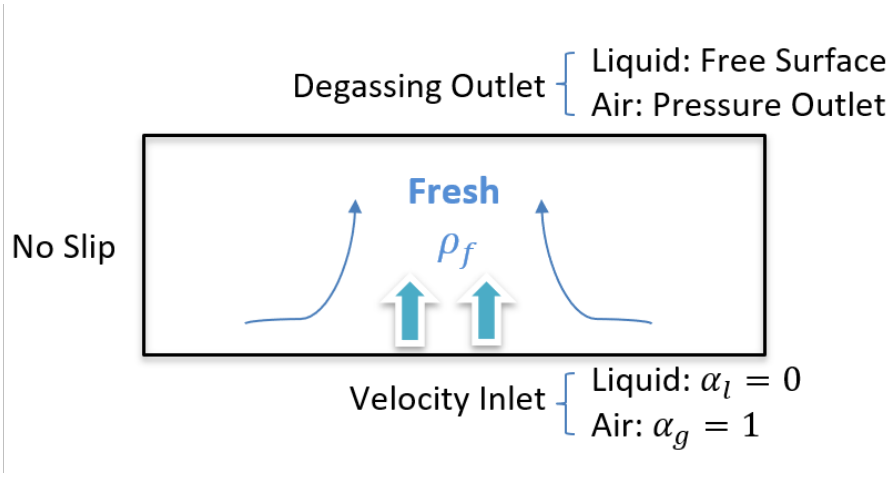

Figure 4-2: A schematic view of the domain setup

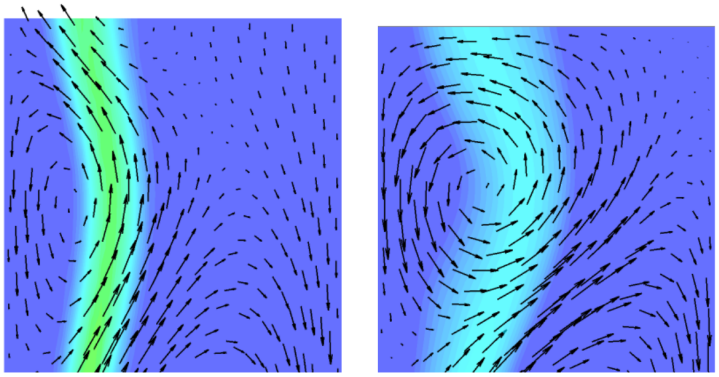

Figure 4-3: Comparison of the pressure outlet boundary condition (left) and degassing boundary condition (right) done by Nygren [7].

seen from the velocity contour, the pressure outlet boundary can not keep the liquid phase from leaving the top. In order to ensure the convergence of mass conservation, the liquid will then be created inside the domain. Such a process will cause a diminish of the salt water in the simulation of the fresh-salt water system and ends up in filling the system with all fresh water, as shown in Appendix Fig.A-11.

A possible alternative would be to extend the domain with a region of air on top of the liquid water. A pressure outlet boundary condition can then be selected at the top of the region. However, this would require a more extensive domain with a higher resolution of cell size, leading to higher computation times and increasing the chance of divergence. An unstable result found by employing this method is presented in Appendix A-2-2.

4-4 Results

In this section, the simulation results for a bubble screen in a fresh-fresh water system simulations using the "laminar" Euler-Euler model will be displayed and discussed. Firstly, a

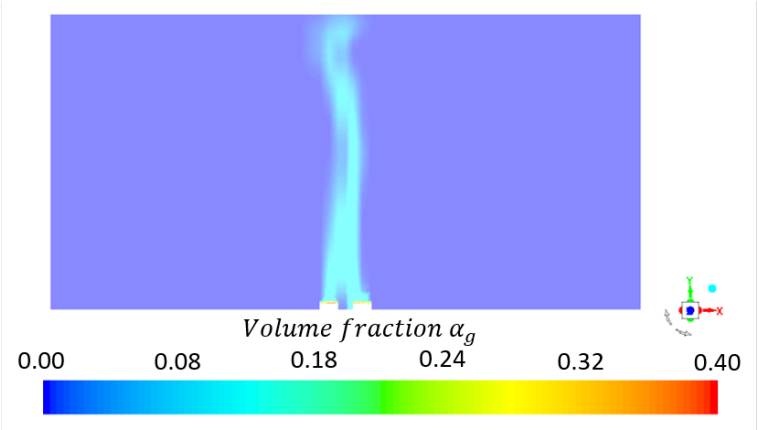

Figure 4-4: A slice of the air volume fraction at $t = 25\ s$ in the midplane at $z = 0.25\ m$, with the air flow rate of $55.96\ L/min$ using the "laminar" Euler-Euler method in Fluent 17.2.

qualitative analysis will be conveyed on the entire flow pattern. Then the velocity profiles will be compared with the PIV data and the analytical deduction to study the circulation and the surface current caused by the air injection. Finally, the liquid entrainment will be analyzed through the plume width.

4-4-1 Qualitative Analysis

First, a qualitative analysis will be carried out based on the instantaneous visualizations of the bubble screen in the fresh-fresh water system. The time of the results is chosen at $125s$ when a bubble screen is fully developed. Fig.4-4 shows the volume fraction of air at a small slice right in the middle of the midplane at $y = 0.25m$. It is visible that the bubbles are injected along the two slits at the bottom. The two rows of bubble flow join together to form a dense bubble screen in the end. Also, from this image as well as other screenshots at different times, included in Appendix A-2-3, the bubbles do not rise in a straight manner. A swinging behavior of the bubble screen along the height of the domain can be observed as the bubble screen is easily disturbed by the liquid flow around. The oscillation is more apparent at the top of the domain where a surface current is present.

Fig.4-5 shows a horizontal liquid velocity profile with the air flow rate of $55.96\ L/min$ at the midplane $y = 0.25\ m$. As can be seen, a circulation pattern is formed with the injection of the bubble screen at the midpoint. The bubble screen at the middle entrains the liquid from the bottom to top and gets dispersed at the surface. A surface current is then generated as the liquid spreads to the sides of the domain. Due to the influence of gravity and mass conservation, the liquid sinks to the bottom and flows back to the bubble screen.

A top view of the vertical air velocity, as presented in Fig.4-6, also reveals a swaying behavior of the bubble screen over the width of the domain. A curved line of the highest velocity in the middle of the view illustrates the place of the bubble screen. Apart from that, it is also notable that quite a considerable amount of air leaves the domain in an area larger than the bubble screen. This phenomenon may result in the generation of foam at the surface. An experimental photo of the bubble screen created by the porous stone sparger is also shown in

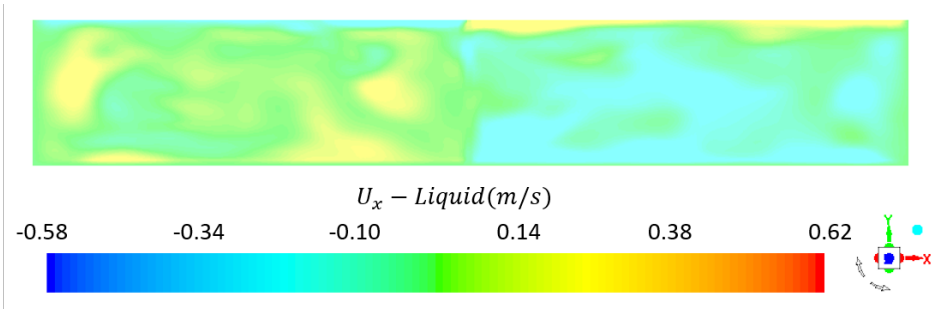

Figure 4-5: Horizontal liquid velocity profile at the midplane at $z = 0.25\ m$, with the air flow rate of $55.96\ L/min$ using the "laminar" Euler-Euler method in Fluent 17.2.

Fig.4-7 for comparison. The distribution of the bubble screen comes in a similar fashion as that of the vertical air velocity.

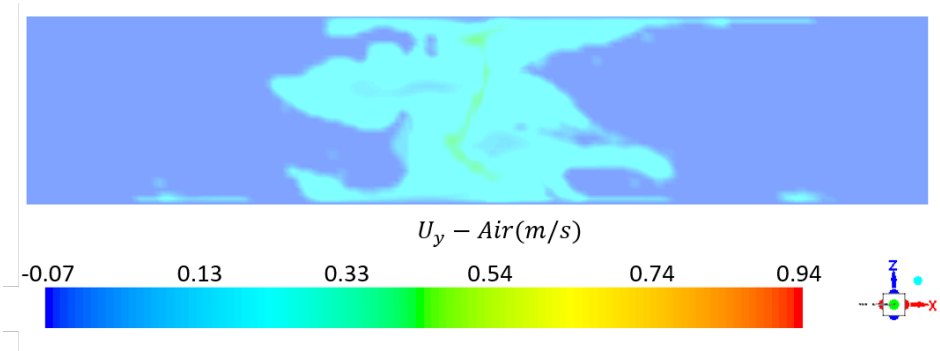

Figure 4-6: Top view of the vertical air velocity at $z = 0.3875\ m$, with the air flow rate of $55.96\ L/min$ using the "laminar" Euler-Euler method in Fluent 17.2.

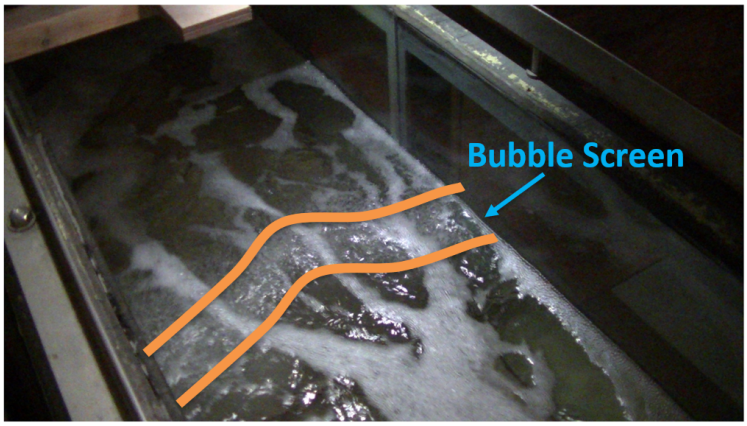

Figure 4-7: Bubble screen created by the porous stone sparger in an experiment at Deltares

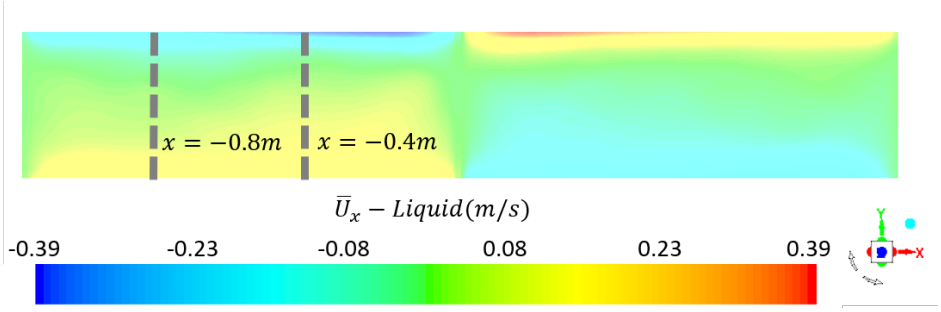

Figure 4-8: Horizontal velocity profile averaged over the entire 125 s at the midplane $z = 0.25\ m$, with the air flow rate of 55.96 L/min using the "laminar" Euler-Euler method in Fluent 17.2.

4-4-2 Circulation

A quantitative analysis is performed on the circulation generated by the bubble screen by comparing the velocity profile with Bulson's empirical correlation and the PIV results of the lab-scale experiments. The time-averaged horizontal liquid velocity is considered along two lines in the midplane of the domain at $z = 0.25\ m$, with a distance of 0.4 m and 0.8 m from the centerline of the bubble screen, indicated by two dashed lines in Fig.4-8 Time averaging is performed over the entire 125 s. The circulation pattern is more obvious in the time-averaged horizontal velocity profile.

Velocity Profiles

The time-averaged liquid horizontal velocity profiles for all three Froude air numbers are extracted at $x = -0.4\ m$ and $x = -0.8\ m$ from the bubble screen, as plotted in Fig.4-9 and Fig.4-10, respectively. The PIV velocity profile is also plotted as a comparison. The experimental data close to the water surface are not taken into account, as the unpredictable wave motion leads to an abnormal and unreliable trend. The plots for each flow rate separately are shown in Appendix A-2-4.

For all the velocity profiles, high negative velocities are found in a small area near the water surface, while lower positive velocities locate in a wide region below. This flow pattern proves a circulation caused by the bubble injection. The negative flow in the top area is acknowledged as a surface current, with a similar thickness of around 0.13 m for all cases, shown as the solid lines in the plots. A slight increase in thickness is observed from $x = -0.4\ m$ to $x = -0.8\ m$ for the simulation data, while the overall velocity magnitude decreases. The higher air flow rate will result in a stronger surface current velocity as expected from Eq.(4.32). For the velocity profiles close to the bubble screen in Fig.4-9, a notable underprediction of the velocity magnitude can be found compared to the experiment, while the overall trend is matched. This deviation becomes smaller farther from the bubble screen as deserved from Fig.4-10, and a better agreement is indicated between the simulations and experiments. The reason is mainly due to the fact that the grid size is not able to resolve all the turbulence scale, as already discussed in the previous section. Liquid motions in small eddies, especially in the area near the bubble screen, cannot be correctly captured with coarse grid size, and thus causes a bias in velocity profiles between the simulations and experiments.

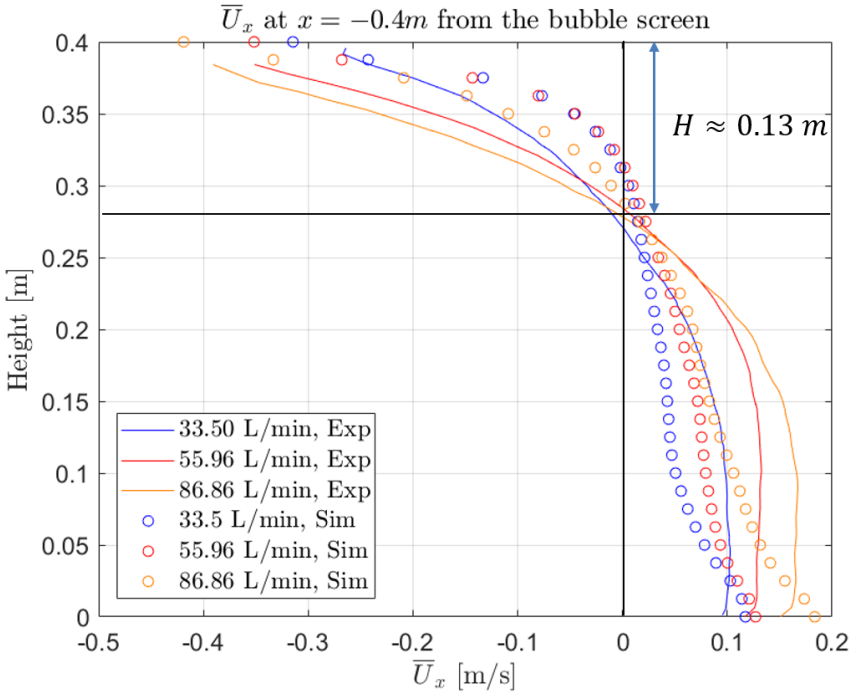

Figure 4-9: Horizontal velocity profiles of all air flow rates averaged over the entire $125\ s$ at $x = -0.4\ m$ from the centerline of the bubble screen in the midplane $z = 0.25\ m$ using the "laminar" Euler-Euler method in Fluent 17.2.

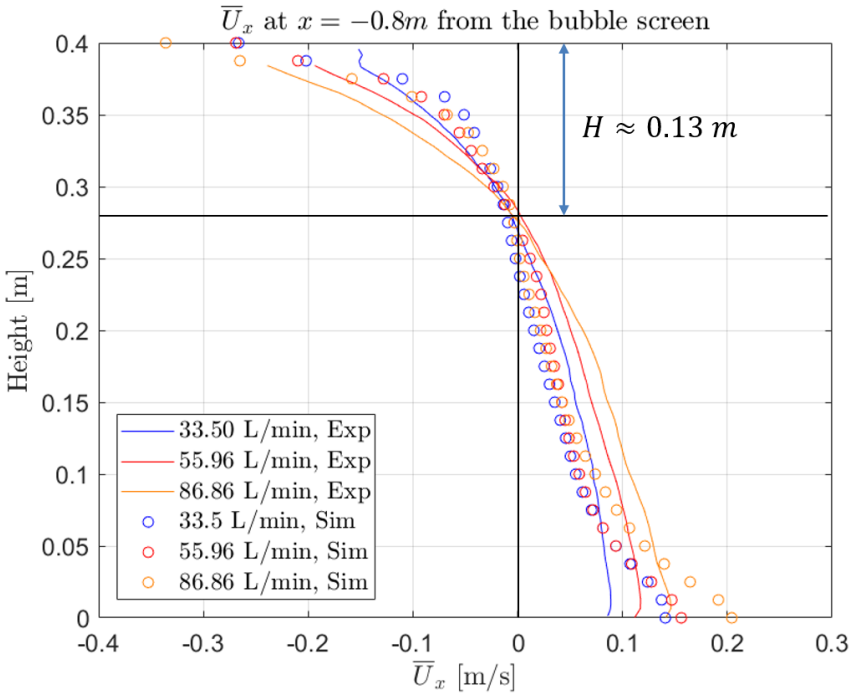

Figure 4-10: Horizontal velocity profiles of all air flow rates averaged over the entire $125\ s$ at $x = -0.8\ m$ from the centerline of the bubble screen in the midplane $z = 0.25\ m$ using the "laminar" Euler-Euler method in Fluent 17.2.

Table 4-4: Horizontal surface velocity magnitude averaged over the entire 125 s at $x = -0.4$ m from the bubble screen

Air flow rate $[L/min]$	Bulson's results $[m/s]$	Simulation results $[m/s]$	Deviation
33.50	0.3202	0.3145	1.76%
55.96	0.3799	0.3516	7.44%
86.86	0.4399	0.4189	4.76%

Based on relevant experiments, Bulson gives the following fomula for the horizontal velocity at a distance equal to the water depth from the upward flow [13]:

$$v_c = 1.46(Q_a g)^{\frac{1}{3}}(1 + \frac{H}{H_0})^{-\frac{1}{3}} \tag{4.32}$$

with Q_a as the air flow rate, H as the water depth, $H_0 = \frac{P_a tm}{\rho_l g}$ as the atmospheric pressure head. The value is compared with the velocity at the surface in Fig.4-8. The results in Table 4-4 show a minor deviation between the simulation and the analytic results. Therefore, the predictions of the surface current velocity are considered reliable.

Grid Size Independence

Different grid sizes are analyzed to investigate mesh independence. Fig.4-10 shows the horizontal velocity computed in three grid sizes, with the air flow rate of 55.96 L/min. As can be seen from the plot, the results of the 9.5 mm grid size simulations are quite similar to the 12.5 mm grid simulation results. The 9.5 mm grid size obtains a more reliable result at $x = -0.4$ m as the surface current thickness is close to the experiments, while the grid size of 12.5 mm corresponds better at $x = -0.8$. However, the grid size of 25 mm shows less accordance with the PIV data. It can be concluded that the Euler-Euler approach is quite sensitive to the mesh grid size, as refining from 25 mm to 12.5 mm significantly improves the results. Further refining the grid gives a weak influence on the prediction. It is also remarkable that refinement should be managed especially near the bottom wall, which will be explained in detail in Chapter 5.

Bubble Diameter Independence

The bubble diameter mainly impacts the drag force in the Euler-Euler approach. A bubble diameter twice the size than that in the experiment is also tested to study the sensitivity. The horizontal velocity profiles with the air flow rate of 55.96 L/min are shown in Fig.4-11. Almost no difference is found between these two cases, except for a tiny decrease in the surface current velocity. Therefore, for the simulations in a lab-scale, the bubble size can be assumed to have little effect. Nevertheless, when scaling up to a large scale, the change in bubble diameter owing to pressure variation along the water depth may result in an essential factor for the simulation.

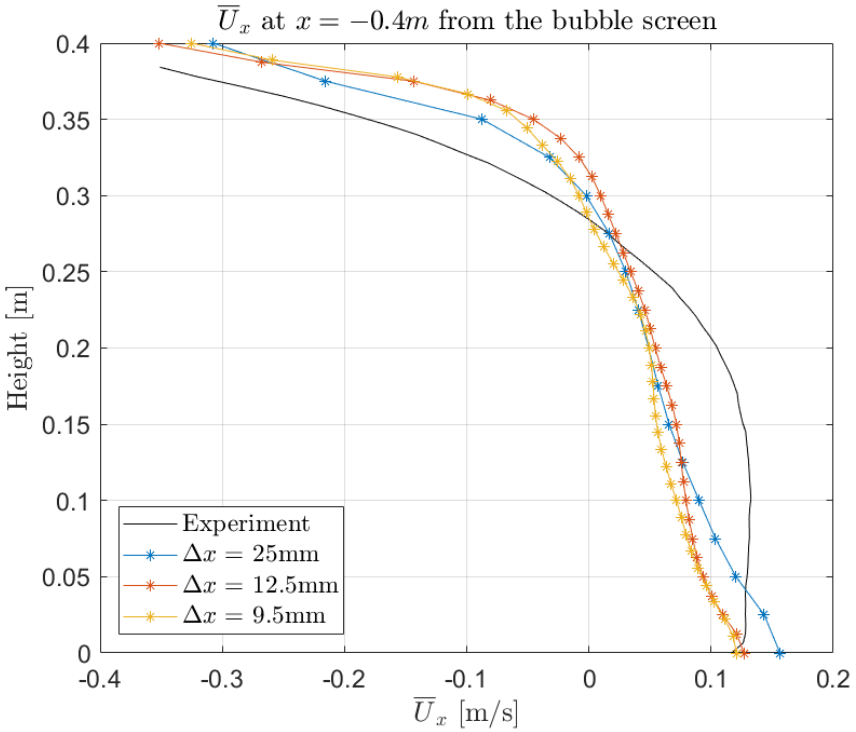

(a) Mean velocity averaged over the entire 125 s at $x = -0.4$ m from the bubble screen.

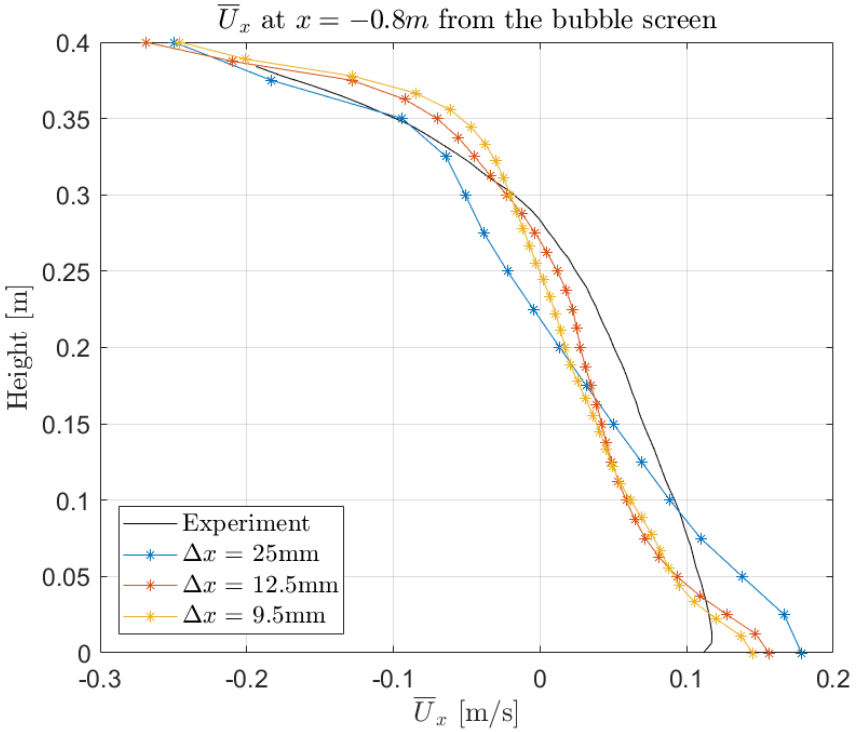

(b) Mean velocity averaged over the entire 125 s at $x = -0.8$ m from the bubble screen.

Figure 4-11: Horizontal velocity profiles in the midplane $z = 0.25$ m computed in different grid sizes, with the air flow rate of 55.96 L/min using the "laminar" Euler-Euler method in Fluent 17.2.

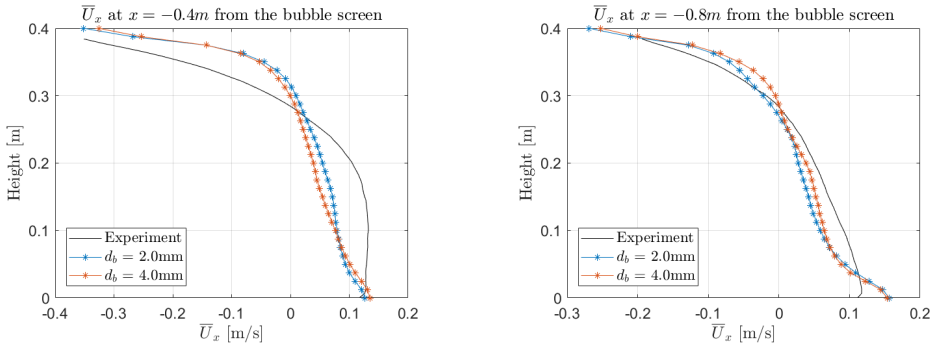

(a) Mean velocity averaged over the entire 125 s at $x = -0.4m$ from the bubble screen.

(b) Mean velocity averaged over the entire 125 s at $x = -0.8m$ from the bubble screen.

Figure 4-12: Horizontal velocity profiles of different bubble diameters in the midplane $z = 0.25m$, with the air flow rate of 55.96 L/min using the "laminar" Euler-Euler method in Fluent 17.2.

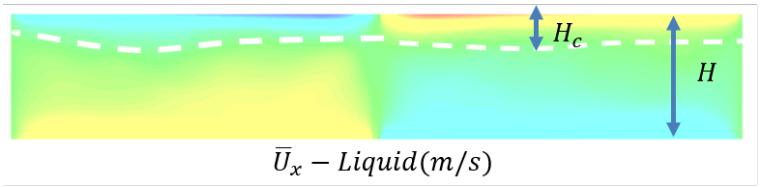

Figure 4-13: Horizontal velocity profiles averaged over the entire 125 s with a sketch of the surface current thickness in the midplane $z = 0.25$ m, at the air flow rate of 55.96 L/min using the "laminar" Euler-Euler method in Fluent 17.2.

4-4-3 Surface Current Thickness

The surface current thickness refers to the height of the horizontal current at the water surface caused by the air injection. Previous experiments have confirmed that the surface current thickness is generally independent of airflow rate and bubble size. An empirical correlation proposed by Bulson shows a logarithmic relationship to the water depth as $H_c/H = k_c * \ln(1 + H/H_0)$, with the constant $k_c = 0.32$ determined from experimental data [13]. Together with the measurements from the Delft Hydraulics Laboratory, Abraham et al. then approximate the equation as $H_c/H = k_c$ with $k_c = 0.25$ [2].A review done by Wen and Torrest mentions that k_c is in the range of $0.25 - 0.33$ [18]. Fanneløp finds a linear increase of the surface current thickness as function of distance from the bubble screen [19]. The increase in the surface current thickness is also detected in the simulation, as shown in Fig.4-12. The white dashed line represents the location where the time-averaged horizontal velocity over the entire 125s equals zero. The increase can be explained by mass conservation, as the surface current velocity decreases away from the bubble screen. The surface current constant can then be calculated based on the average current height over the domain length:

$$k_c = \frac{\overline{H_c}}{H} \tag{4.33}$$

The current height is averaged over the whole midplane, except for the area near the wall

Table 4-5: The surface current contant k_c of simulations and the experiments

Air flow rate $[L/min]$	Sim. k_c	Exp. k_c
33.50	0.313	0.283
55.96	0.266	0.270
86.86	0.313	0.311

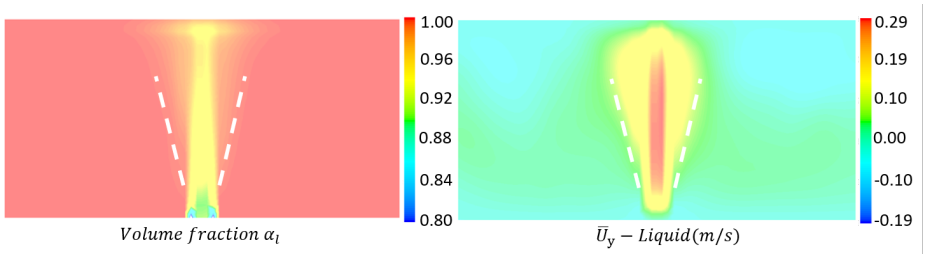

Figure 4-14: Liquid volume fraction plot (left) and the vertical velocity (right) averaged over the entire 125 s in the midplane $z = 0.25$ m with a sketch of the plume width, at the flow rate of 55.96 L/min using the "laminar" Euler-Euler method in Fluent 17.2.

or the bubble screen. The calculated values for the surface current constant k_c based on the simulations and obtained from the PIV measurements are listed in Table 4-5. It can be seen that all the values for the surface current constant k_c fall within the range of values from the literature. Approximate $k_c \simeq 0.3$ is reached for all the porous stone spargers. It is interesting that both for simulations and the experiments, the thinnest surface current thickness is reached for air flow rate equal to 55.96 L/min, corresponding to a Froude air number close to 1.

4-4-4 Entrainment

The entrainment of liquid in the bubble screen is investigated to study its performance as a mixer. The rate of entrainment is determined by the gradient of the plume width. So as to get the plume width, a time-averaged volume fraction is chosen with the liquid volume fraction of 0.999 as a cutoff. A sketch of the plume width is indicated by the dashed lines in Fig.4-13. The regions near the sparger and the water surface are not considered since the air injecting at the inlet and the surface current will interfere with the entrained process. A time-averaged vertical velocity profile of the liquid phase is also displayed for reference.

The plume widths for all air flow rates over the domain height are plotted in Fig.4-14. The dashed line represents the linear regression of the data. It is evident from the linear fit that the plume width increases linearly with the domain height. To further compare the rate of entrainment for all cases, the vertical gradients of the plume width are indicated in Table 4-6. The trend of the rate is similar to the surface current velocity. It can be concluded that a high air flow rate will result in a large liquid upward velocity, and thus entrains a significant amount of water towards the top surface. After being thoroughly mixed inside the plume, this water will end up as a surface current towards the sides of the tank at fast speed. Therefore, it seems the increase of air flow rate will lead to a wide plume width and a high rate of entrainment, which means more fluid from both sides of the bubble screen is going

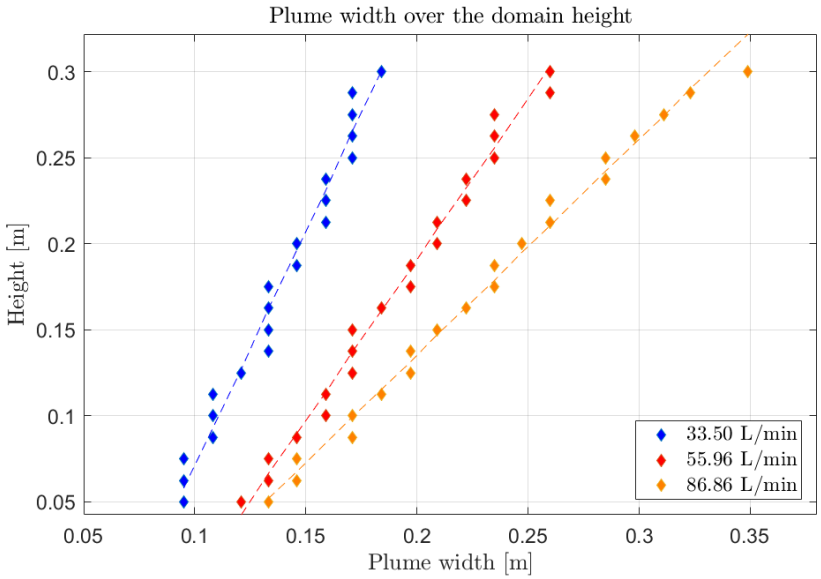

Figure 4-15: Plume width over the domain height

Table 4-6: The rate of entrainment for all air flow rate

Air flow rate $[L/min]$	Rate of entrainment
33.50	0.3657
55.96	0.5341
86.86	0.7972

to mix at the water surface. In other words, this also means less liquid is flowing across the bubble screen in the bottom area. Other characteristic parameters of a bubble plume, such as the entrainment coefficient, defined as a ratio of the horizontal velocity of the entrained liquid to the upward liquid velocity, are not further discussed as they provide less valuable information on the bubble screen.

4-5 Conclusions and Remarks

In this chapter, the Euler-Euler approach is introduced in detail and the "laminar" model is used to simulate the bubble screen behavior in a fresh-fresh water system. The numerical model with the porous stone spargers is validated with PIV data collected from Deltares experiments, as well as some empirical relations from literatures. The porous stone generates a dense bubble screen with a circulation pattern formed in the liquid phase. Simulations of the bubble screen produced by the PVC tube does not meet the actual inlet velocity, with the inlet area as a slit instead of small orifices.

The circulation pattern is further investigated based on the time-averaged horizontal liquid velocity profiles. An underestimation of the velocity magnitude can be observed compared to the PIV measurements for all cases, while the overall trend is matched. The increasing

air flow rate will result in a stronger surface current velocity. An agreement with the results from Bulson is found in the horizontal surface velocity. A larger bubble size nearly has no influence on the velocity profiles, while the velocity results are quite sensitive to the grid size. Refining from a coarse mesh to a fine mesh significantly improves the results. But further slightly refining the grid gives a weak influence on the prediction. However, to fully resolve the small scale eddies and turbulent velocity fluctuations, a grid size equal to the Kolmogorov length scale should be reached for the "laminar" model.

Regarding the surface current height, the surface current constants of all cases match well with previous literature, being equal to nearly 30 percent of the water depth. For the entrainment of the bubble screen, the plume width grows linearly with the domain height. An increasing air flow rate will lead to a larger plume width and a higher rate of entrainment, which means more fluid from both sides of the bubble screen is going to mix at the water surface, whereas less liquid is flowing across in the bottom area.

It can be concluded that the present model is successful in reproducing a bubble screen in a fresh-fresh water system. In the next chapter, the mass transport equation for salt concentration, together with the concentration-density relation for salt water, will be added for the liquid phase. A bubble screen in a fresh-salt water system will then be investigated.

Chapter 5

Bubble Screen In A Fresh-Salt Water System

5-1 Introduction

Bubble screens are widely used in water quality control, such as pneumatic oil barriers and barriers preventing plastic pollution [58]. Apart from those applications, the use of bubble screens for mitigating the salt intrusion has also been studied over decades. Installations near navigation locks have been worked successfully to reduce the seawater intrusion. Regarding the required time and other resources needed for a field study, lab-scale experiments and relevant simulation models are more desired for the design of bubble screens in different conditions. In this chapter, the simulation of a bubble screen in a fresh-salt water system will be presented. The dimensionless number of the bubble screen will be introduced first as a characteristic parameter for the system. The dynamic behavior of the bubble screen is modeled with the Euler-Euler approach, in combination with a mass transport equation for the salt concentration and an equation of state that relates the fluid mass density to the local salt concentration. Results will be compared with some empirical correlations from literature and the dye measurements described in Chapter 2. Finally, conclusions and remarks will be given on the simulation of salt intrusion in the presence of the bubble screen.

5-2 Theory

Froude Air Number

The Froude air number is a dimensionless number first introduced by Abraham and Van der Burgh for scaling air bubble screens. The derivation is mainly based on two energy balance equations. For the salt intrusion, as shown in Fig.5-1, it is assumed that the loss of potential energy from the salt water at position four transfers to the kinetic energy of the same current

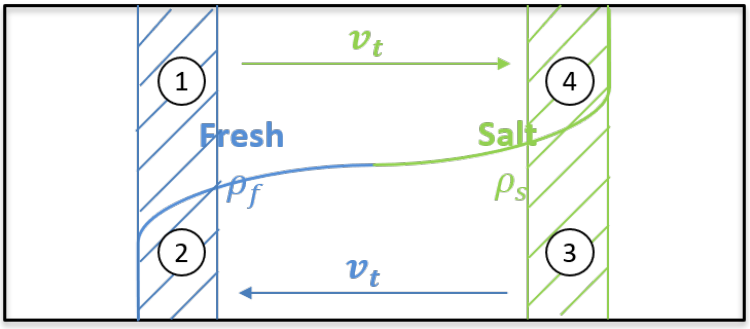

Figure 5-1: A schematic picture of a gravity current.

velocity for both fresh and salt water:

$$E_p = (\Delta\rho g \frac{1}{2} H) * (\frac{1}{2} H L_z v_t \Delta t) \tag{5.1}$$

$$E_k = 4 * \left[\frac{1}{2}\overline{\rho}\left(\frac{1}{2} H L_z v_t \Delta t\right) v_t^2\right] \tag{5.2}$$

where Δt represents a short period of time, $\Delta\rho$ represents the density difference between fresh and salt water, L_z is the domain width and H is the water depth. The mean density of fluids $\overline{\rho}$ is normally considered as the salt water density as $\frac{\Delta\rho}{\overline{\rho}} \ll 1$. The gravity current velocity can then be determined by $E_k = E_p$:

$$v_t = (\frac{1}{4}\frac{\Delta\rho}{\rho_{l,s}} g H)^{\frac{1}{2}} \tag{5.3}$$

For the case of bubble screen, assuming that the air is injected at a pressure that is just sufficient to overcome the hydrostatic head while the temperature keeps constant, the volume of air at a distance a from the water surface is:

$$V = \frac{H_0}{H_0 + a} V_{atm} \tag{5.4}$$

with $H_0 = \frac{P_a tm}{\rho_l g}$ as the atmospheric pressure head and V_{atm} as the volume of air at the water surface. The total energy required for a fully developed bubble screen can be derived as:

$$E_{air} = \rho_l g \int_0^H V da = \rho_l g H_0 \ln(1 + \frac{H}{H_0}) Q_a L_z \Delta t \tag{5.5}$$

where Q_a is the air flow rate per unit width of the domain. The energy transferred to the liquid mainly contributes to the kinetic energy of the surface current at both sides of the bubble screen:

$$E_{surf} = \int_0^T \rho_l v_c^2 * v_c L_z \Delta t * dh = \rho_l T L_z \overline{v}_c^3 \Delta t \tag{5.6}$$

using $\overline{v}_c$ as the mean velocity of the surface current and T as the surface current thickness.

A ratio of η is considered for energy transfer from air to the water as $E_{surf} = \eta E_{air}$. The mean surface current velocity can be acquired as:

$$\overline{v}_c = \left[\frac{\eta H_0 \ln(1 + \frac{H}{H_0})}{T}(Q_a g)\right]^{\frac{1}{3}} \tag{5.6}$$

Table 5-1: Relevant physical properties of the bubble screen fresh-salt simulations.

Parameter	Value	Unit
Ambient Pressure P	101325	Pa
Ambient Temperature T	20.0	$°C$
Fresh water density $\rho_{l,f}$	998.21	kg/m^3
Salt water density $\rho_{l,s}$	1019.21	kg/m^3
Liquid dynamic viscosity μ_l	$1.003 * 10^{-3}$	$kg/(m * s)$
Salt diffusivity D	$1.6 * 10^{-11}$	m^2/s
Gas density ρ_g	1.204	kg/m^3
Gas dynamic viscosity μ_g	$1.825 * 10^{-5}$	$kg/(m * s)$
Gravity acceleration g	9.81	m/s^2
Surface tension coefficients γ	$72.86 * 10^{-3}$	N/m
Bubble diameter d_b	2.0	mm

Previous experiments by Bulson and the Delft Hydraulics Laboratory shows the surface current thickness only depends on the water depth [2, 13]. The measurements also reveal that surface current velocity is independent of the water depth, as already presented in Chapter 4. Therefore, the mean surface current velocity can be expressed by:

$$\overline{v}_c = K_c(Q_a g)^{\frac{1}{3}} \tag{5.7}$$

with K_c as an empirical constant of around $1.2 - 1.46$. The Froude air number, serving as a ratio of the kinetic energy from the rising bubbles to the potential energy of the gravity current, can be converted to the ratio of the mean surface current velocity to the gravity current velocity:

$$Fr_{air} = \frac{(Q_a g)^{\frac{1}{3}}}{(\frac{\Delta\rho}{\rho_{l,s}} g H)^{\frac{1}{2}}} \tag{5.8}$$

5-3 Simulation Setup

The simulation of the bubble screen in the fresh-salt water system is achieved by using the mass transport equation for the salt concentration and a concentration-density relation in the Euler-Euler approach, which can be recognized as a mixing of two miscible fluids in the presence of bubble screen. The physical properties are listed in Table 5-1. The geometry of the domain is identical to the lab-scale experiments with a grid size of 12.5 mm. The boundary conditions are the same as for the fresh-fresh case. Different Froude air numbers are chosen apart from $0.63 - 1.15$ for comparison of the bubble screen mitigating performance, as shown in Table 5-2. The "laminar" model is used here for turbulence modelling since the LES model cannot be used in combination with the Euler-Euler approach in Fluent 17.2. Results of other turbulence models, including the standard $k - \epsilon$ model and the $k - \omega$ SST model, are shown in Appendix A-3-1.

Table 5-3 presents all the numerical settings. Each case is running in a fresh-fresh water system in the first 30 s for a fully developed bubble screen. After reaching a steady state, half

Table 5-2: Froude air numbers and corresponding air flow rates for the bubble screen fresh-salt simulations and experiments.

Num. Fr_{air}	Num. flow rate $[L/min]$	Exp. Fr_{air}	Exp. flow rate $[NL/min]$
0.63	17.25	-	-
0.70	24.00	-	-
0.78	33.50	0.80	33.50
0.93	55.96	0.95	55.96
1.08	86.86	1.08	86.86
1.15	105.53	-	-

Table 5-3: Numerical setting of the bubble screen fresh-salt simulations.

Parameter	Value
Domain size $[L_x \times L_y \times L_z]$	$2.4\ m \times 0.4\ m \times 0.5\ m$
Grid cells	$192 \times 32 \times 40$
Time step	$0.01\ s$
Pretreatment time	$30\ s$
Full simulation time	$150\ s$

of the domain will be patched with the salt water for the following 120 s. Full simulation time is set to 150 s, while only the last 120 s will be taken into consideration. For simplification, the change in surface tension due to salt concentration is neglected, as already mentioned in Chapter 2. However, previous work by Mathias Bostrom et al. points out that the surface tension shows a strong dependence on the ion pair, and the increase of surface tension is proportional to the concentration of salt [31]. Further study about this issue may be desired for large scale simulation.

5-4 Results

In this section, the results of the bubble screen fresh-salt simulations will be displayed and discussed. First, screenshots at different time steps will be compared with dye measurements to study the mixing pattern at different Froude air numbers. Then the mitigating performance will be quantified by the volume-averaged concentration and the salt transmission factor. Finally, the Lacey's Mixing Index will be adopted to study the local mixing in the presence of the bubble screen.

5-4-1 Qualitative Analysis

Qualitative analysis will be carried out based on the instantaneous visualizations of the bubble screen in the fresh-salt system. Screenshots of the concentration profile for the air flow rate of 86.86 L/min in the midplane of the domain are provided in Fig.5-2, as a comparison with the dye coloring measurement results. Several time steps are chosen within the first 40 s and also

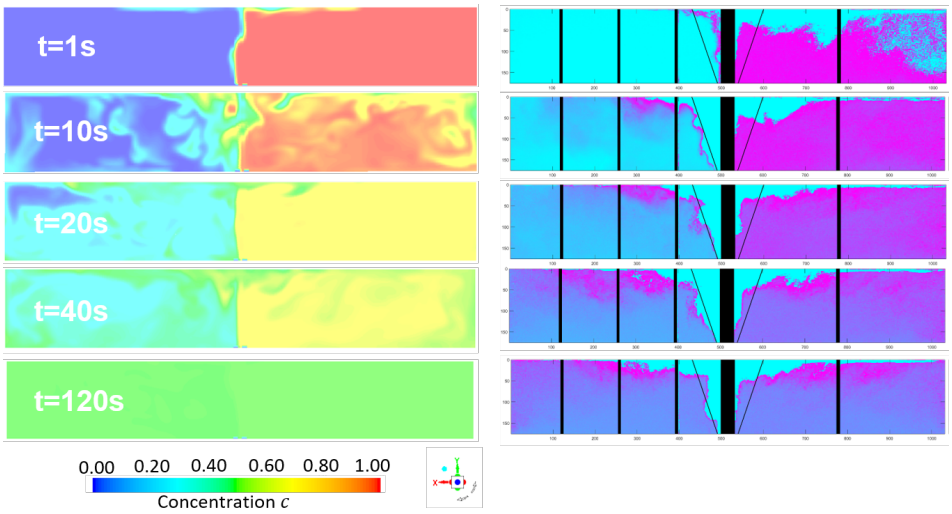

Figure 5-2: Comparison of the concentration profiles between simulations (left) and experiments (right) at several time steps, with the air flow rate of 86.86 L/min in the midplane $z = 0.25m$ using the "laminar" Euler-Euler method in Fluent 17.2.

the final 120 s. Screenshots of other time steps and air flow rates are included in Appendix A-3-2. As can be seen in the pictures, the simulation profiles match well with the experimental results. As for the initial condition on the right side in the dye measurements conducted at Deltares, the spreading of the bubbles caused by removing the lock cannot be illustrated on the greyscale image, and thus leads to a blank on the surface. The same situation can also be noticed in the middle, where the bubble screen forms, as the gas phase cannot be illuminated and recorded. From the comparison, the bubble screen prevents both sides of the fluids from mixing at first. However, the salt water gradually intrudes into the fresh side through the surface current at the top of the domain. A thoroughly mixed situation is reached at the end, where there is no concentration difference between both sides of the domain.

Velocity vector profiles of the same flow rate are also displayed in Fig.5-3(a) for a clear observation of the flow pattern. A small circulation occurs near the bubble screen on the fresh side, because a higher density of the entrained water cause it sinks faster. On the other side, the entrained water at the salt side is lighter than the salt water and tends to move farther from the bubble screen. Such a phenomenon is also expected from the theory of the pneumatic barrier, as shown in Fig.5-3(b), which emphasizes a mixing at the boundaries of the small eddy as well [2, 3].

Salt Tongue

While the salt water is likely to intrude through the surface current generated by the bubble screen, a salt tongue is also found for low Froude air numbers both for simulations and experiments. This represents that the bubble screen can not prevent the salt intrusion due to gravity current. Viscous wall unit is employed to study the grid resolution near the wall. A horizontal maximum shear stress at the gravity current is about $\tau_w = 1.5 * 10^{-2}$ Pa. The

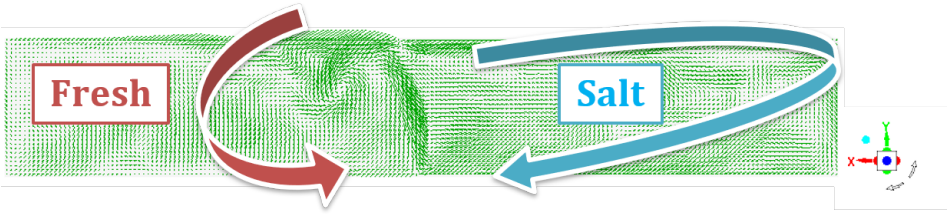

(a) Velocity vectors and corresponding circulations at $t = 10\ s$, with the air flow rate of 86.86 L/min in the midplane $z = 0.25\ m$ using the "laminar" Euler-Euler method in Fluent 17.2.

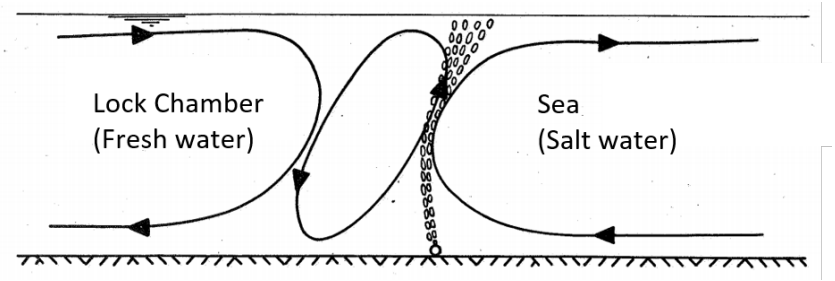

(b) Theoretical flow pattern near the pneumatic barrier [2].

Figure 5-3: Comparison of the flow pattern between the simulation and the theory.

shear velocity can be calculated as:

$$u_w = \sqrt{\frac{\tau_w}{\rho_{l,s}}} \tag{5.9}$$

with a value of $3.84 * 10^{-3}\ m/s$. The viscous wall unit can then be calculated as:

$$\sigma_v = \frac{\nu_{l,s}}{u_w} \tag{5.10}$$

$y+$ as a ratio of the grid size to the viscous wall unit should be kept less than 5 for the laminar model in the near-wall region, as already explained in Chapter 3. Therefore, the required grid size should be 1.31 mm, which means further refinement needs to be made in the mesh near the wall. This ratio also explains the velocity profiles shown in Fig.4-10, where a refined grid size has a better prediction near the wall in correspondence to the experimental results.

5-4-2 Mitigating Performance

In order to quantify the performance of the bubble screens as a mitigating measurement, the concentration c is averaged over the entire fresh side (left half of the domain). Fig.5-5 plots the volume-averaged concentrations over time for Fr_{air} from 0.63 to 1.15. The concentration profile of the gravity current case is also included as a reference, representing the case without the presence of the bubble screen as $Fr_{air} = 0$. It can be seen that the bubble screen successfully acts as a pneumatic barrier since the salt water on the left side is initially less than that without any measurements. The air injection with a high flow rate tends to achieve similar performances, whereas the air flow rate of 53 L/min seems to perform best when zooming in. However, the bubble screen with a low Fr_{air} does not work ideally with a

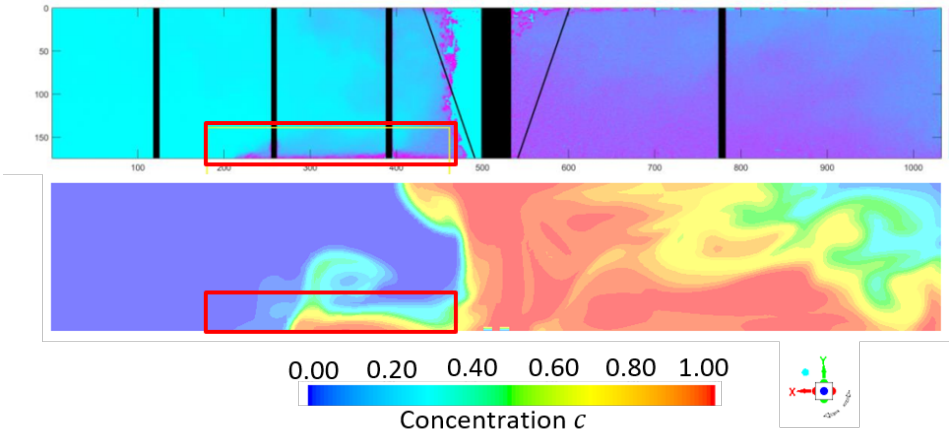

Figure 5-4: Salt tongue with $Fr_{air} = 0.8$ in experiments (top) and simulations (bottom) at $t = 8\ s$, with the air flow rate of 33.50 L/min in the midplane $z = 0.25\ m$ using the "laminar" Euler-Euler method in Fluent 17.2.

concentration beyond 0.5 before a steady state is reached. It can be concluded from the overview that the bubble screen can only mitigate the process of salt intrusion rather than stop it.

Validation with Lab-scale Experiments

Two sets of lab-scale experiments are conducted for each air flow rate. Fig.5-6 presents the comparisons of the three initial air flow rates with the corresponding dye measurement results, respectively. For experimental results, the noisy curves are generated in the plots mainly because of the mask region for the aluminum support and bubble screen that is accounted as 50% of dye all the time. Also, inaccuracy will be caused by the environmental disturbance on the light that illuminates the grayscale images. Due to this reason, the second set of experimental results in Fig.5-6 a) is considered incorrect since the volume-averaged concentration reaches a final value below than 0.5. For all other cases after the measurements, the water has been confirmed as a mixture with a uniform distribution of dye. A significant discrepancy appears between the simulations and the experiments from 20 s to 40 s. During this time, the surface current flow hits the sides of the domain and flows back to the bubble screen. The current grid size may not be able to resolve the influence of the reflection on the stream pattern, as well as on the dynamic of the bubbles. However, for other periods, the simulation results match quite well.

Salt Transmission Factor

The salt transmission factor is introduced by Abraham et al. to describe the effectiveness of various mitigating measure. It is defined as a ratio of the salt intrusion with mitigating measures to that without any measures:

$$\eta = \frac{salt\ intrusion\ with\ mitigating\ measures}{salt\ intrusion\ without\ mitigating\ measures} \tag{5.10}$$

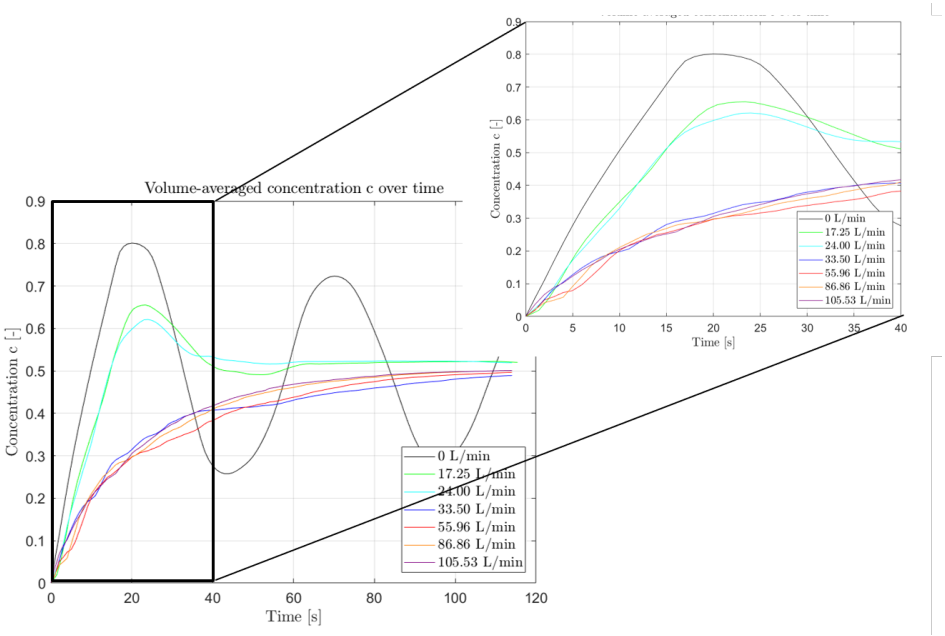

Figure 5-5: Volume-averaged concentrations over the entire simulation time with a zoom-in view of 0-40s using the "laminar" Euler-Euler method in Fluent 17.2.

A semi-empirical correlation based on a field study is used to specify the salt transmission factor as function of the Froude air number:

$$\eta = \left(-0.86\theta + \frac{0.185}{\theta} + \theta^3\right) * 100\% \pm 5\% \tag{5.11}$$

with $\theta = 0.4 * Fr_{air}$. A 5% deviation is included in the equation, plotted as the dashed line in Fig.5-7. Field tests results collected by Uittenbogaard et al. are also shown as the dots [15]. The salt transmission factor for the simulations and the lab-scale experiments is calculated by averaging the concentration c over the first 10 s, before the reflection of the surface current in order to claim comparison with Abraham's correlation and field tests where no sidewalls are presented. Otherwise, the bubble screen will again prevent the salt water in the fresh side flowing back to the salt side.

Overall, both the salt transmission factors of the dye measurements and the simulations fall beyond the semi-empirical correlation and most of the field tests but do agree well with each other. Since the semi-correlation is dependent on the field-study results, the dense plume created by the porous stone spargers and the small size of air bubbles may not be able to prevent the salt intrusion efficiently. Also, the reflection caused by the sidewalls may also push the salt water moving torwards fresh side, whereas the small circulation on the fresh side prevent the intruding salt water from flowing back. Further simulations are conducted at a relatively lower and higher Froude air number to study the trend. It can be seen that for a Froude air number below 1, the salt transmission factor declines with increased air flow rates, while at a higher Froude number, the simulation and experiment results illustrate an upward leaning. The energy balance can explain this. The kinetic energy supplied by the air injection is equal to the potential energy of the gravity current at $Fr_{air} = 1$. Either increase or decrease in the kinetic energy will accelerate the mixing process. The semi-empirical

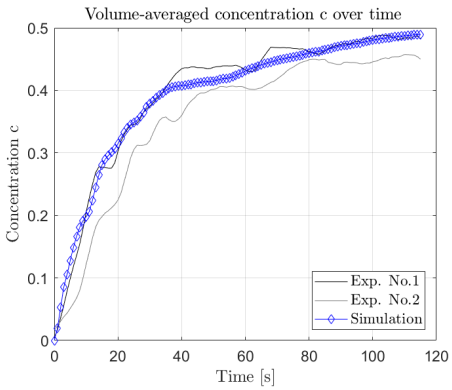

(a) Air flow rate of 33.50 L/min

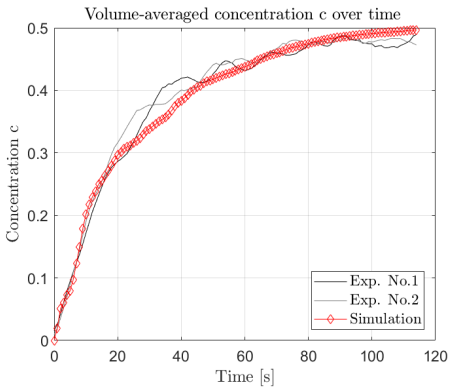

(b) Air flow rate of 55.96 L/min

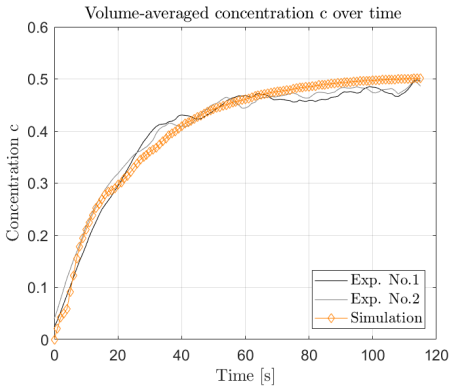

(c) Air flow rate of 86.86 L/min

Figure 5-6: Volume-averaged concentrations for fresh side over time

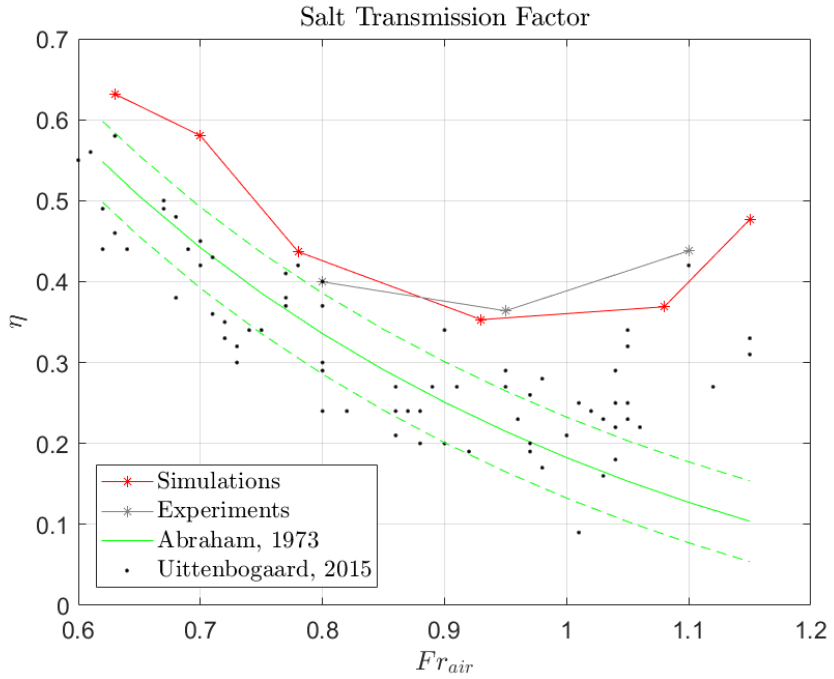

Figure 5-7: Salt transmission factor η as a function of Fr_{air} using the "laminar" Euler-Euler method in Fluent 17.2.

prediction continues a downward trend because the theory neglects the mixing in the upward flow caused by the pneumatic barrier, while the salt transmission factor for the field tests spreads beyond the correlaton for Fr_{air} over 1. To conclude, a bubble screen with a Froude air number in the range of $0.8 - 1.1$ seems to be most efficient for mitigating salt intrusion as also found in a previous study at Deltares [4].

5-4-3 Local Mixing

In order to investigate the salt intrusion alongside the bubble screen, a study on the local mixing is performed. Currently, many suitable mixing indices are available that can be used to analyze mixing behavior. Typically, investigations of mixing indices are based on the statistical method, but other methods relating to photometric and kinetic approaches are also applied [59]. Here, a primary method using the Lacey's Mixing Index is employed [60].This index introduced by Lacey divides the area of interest into N simulation grid cells. The variance of σ^2 for the concentration c in each cell can be expressed by:

$$\sigma^2 = \frac{\Sigma_{i=1}^{N}(c_i - c_m)^2}{N-1} \tag{5.12}$$

where c_i is the concentration in each cell, c_m is the concentration of the mixed state. Then the Lacey Mixing Index can be defined as:

$$M = \frac{\sigma_{max}^2 - \sigma^2}{\sigma_{max}^2 - \sigma_{min}^2} \tag{5.13}$$

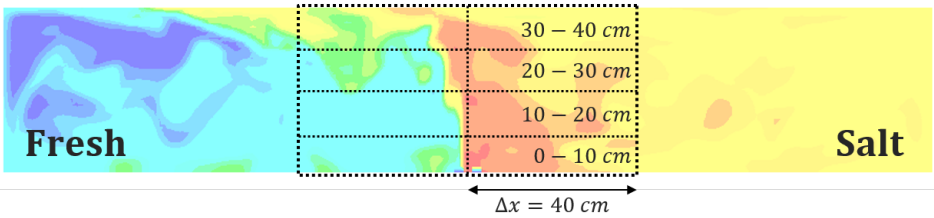

Figure 5-8: A sketch of the area divided for the study of the LMI in the midplane $z = 0.25\ m$

with σ^2_{max} and σ^2_{min} denotes the maximum variance and the minimum variance, respectively. For the current case, these parameters represent the unmixed states and fully mixed state:

$$\sigma^2_{max} = \frac{N}{N-1} * c^2_m = \frac{N}{N-1} * \frac{1}{4} \tag{5.14}$$

$$\sigma^2_{min} = 0 \tag{5.15}$$

Here, c_m is 0.5 at the complete mixing state of the fresh and salt water. Because it is defined through the unmixed state and fully mixed state, the LMI is capable of describing the degree of mixing in the selected area. The LMI close to 1 represents a fully mixed situation, while the index equal to 0 means completely unmixed or segregated from each other. The limitation of this method is also obvious, as only binary mixtures like the fresh-salt water system can be considered. An area with a distance of 40cm to the pneumatic barrier on two sides is analyzed. This area is divided into eight pieces with a height of 10 cm, with each containing N grid cells as sketched in the midplane in Fig.5-8.

The LMI is extracted for both fresh and salt sides over the first 40 s, as displayed in Fig.5-9. Here several time instances with a resolution of 10 s are taken for intuitive plotting, with the first 10 s is shown in detail. The LMI on the fresh side at three Froude air number equal to $0.80, 0.95, 1.10$ are shown here, with the plots for the other side as well as other air flow rates can be found in the Appendix A-3-4. It is recognized that, for a low Froude air number, the salt water mostly intrudes at the bottom 10 cm, while for higher Froude air number, the salt intruding through the surface current plays a dominant role. These plots further prove that the pneumatic barrier can prevent the salt intrusion through the bottom with a larger air flow rate. But in the meantime, the screen will enhance the mixing at the top surface.

5-5 Conclusions and Remarks

In this chapter, the Froude air number is introduced to describe the bubble screen in a fresh-salt water system. The Euler-Euler approach and a mass transport equation in the liquid phase are employed for the simulation, which will be introduced in detail in Appendix B-1. The surface tension coefficient is assumed to be constant here. But when it comes to a large scale, the concentration of salts will profoundly influence the surface tension coefficient, and thus also affect the drag coefficient and the bubble shape.

From a qualitative analysis of the fresh-salt results, the bubble screen prevents both sides of the fluids from mixing in the first 10-20s. However, as the salt water gradually intrudes into the fresh side through the surface current at the top of the domain, a thoroughly mixed

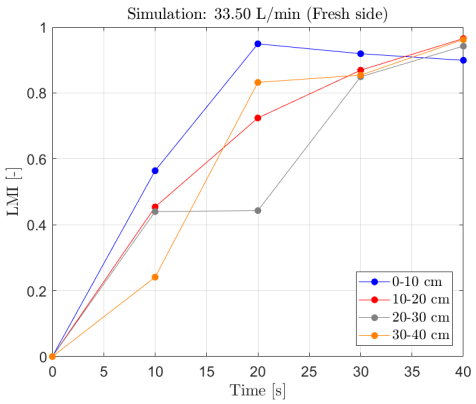

(a) air flow rate of 33.50 L/min

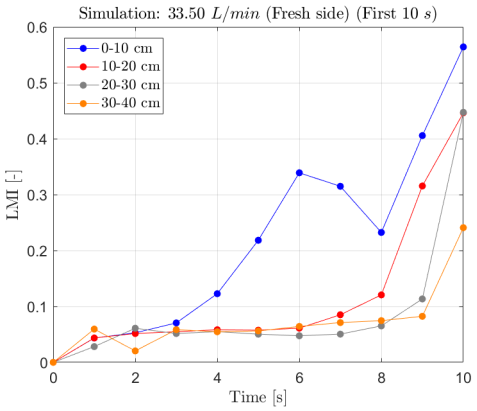

(b) air flow rate of 33.50 L/min for first 10 s

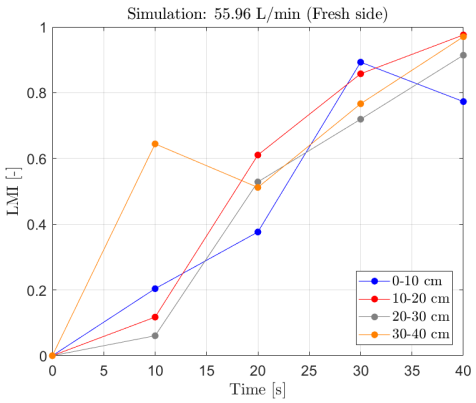

(c) air flow rate of 55.96 L/min

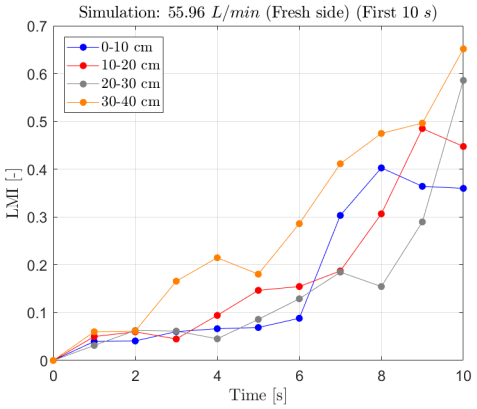

(d) air flow rate of 55.96 L/min for first 10 s

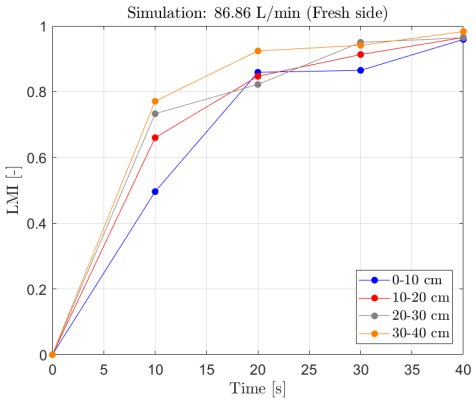

(e) air flow rate of 86.86 L/min

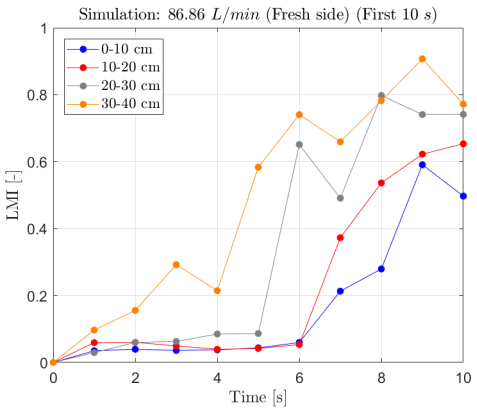

(f) air flow rate of 86.86 L/min for first 10 s

Figure 5-9: The LMI over the 40 s (left) and the first 10 s on the fresh side using the "laminar" Euler-Euler method in Fluent 17.2.

situation is reached in the end. A small circulation is observed near the bubble screen on the fresh side caused by the density difference, which is expected from previous work. At a low Fr_{air}, a salt tongue is likely to occur both for simulations and experiments. According to the viscous wall unit, a refined grid size of around 1 mm is needed near the wall to predict the relevant properties of the salt tongue better.

Regarding the mitigating performance, the volume-averaged concentration profiles on the fresh side show that the salt intrusion is mitigated in the first 20 to 30 seconds compared to the gravity current. A higher Fr_{air} tends to achieve similar performances, among which the air flow rate of 53 L/min ($Fr_{air} = 0.93$) performs best. The bubble screen at a low Fr_{air} does not work ideally. A good agreement is achieved with the dye measurements. The variance between the CFD and dye measurement results may mainly be caused by the reflection of the flow from the domain sides. The current grid size can not fully resolve the influence of the reflection on the stream pattern after the surface current reaches the sides of the domain, as well as on the dynamic of the bubbles.

The salt transmission factor has been calculated based on the first 10 seconds of simulations before the reflection of the surface current. Both the salt transmission factor of the dye measurements and of the simulations fall beyond the semi-empirical correlation. The dense plume and the small size of air bubbles may not be effective to prevent the salt intrusion compared with the field study. In terms of the overall trend, a bubble screen with a Fr_{air} in the range of 0.93 - 1.08 seems to be most efficient for mitigating salt intrusion.

From local mixing results, it is concluded that for a low $Fr_{air} < 0.93$, the salt water mostly intrudes at the bottom area, while for higher $Fr_{air} > 0.93$, the salt intruding through the surface current plays a dominant role. Therefore, the pneumatic barrier can prevent the salt intrusion through the bottom as well as enhance the mixing at the top surface. This phenomenon can also be explained by the Fr_{air}, as the kinetic energy supplied by the air injection equals to the potential energy of the gravity current at Fr_{air} around 1.

It can be concluded that the present model is successful in reproducing a bubble screen in a fresh-salt water system in a lab scale. In the next chapter, several recommendations will be given for future work on bubble screens.

Chapter 6

Conclusions and Recommendations

In this chapter, a summary of conclusion will be delivered on the presented work, and some recommendation will be given for future work on bubble screens to mitigating salt intrusions.

6-1 Modeling the Salt Intrusion

It is shown in Chapter 3 that the LES model and the "laminar" model are successful in predicting the gravity current with the mass transport equation for salt concentration. Several assumptions and approximations here can be further developed in detail.

Firstly, the density of the liquid is considered as a linear relationship with the salinity at constant temperature and pressure. In reality, the temperature and pressure may change with time, and thus an energy equation can be employed to compute the temperature change. The liquid density can then be expressed based on an ideal gas model or even more complicated model [29].

Secondly, the salt diffusivities and the dynamic viscosity are considered as constant here. However, these terms will vary with different salinity and also the diverse compositions of salt in seawater, which is of great importance for flow dominated by turbulent diffusion [37, 35]. It is recommended to consider the salt as a set of dissolved ions, with each of them contributing to the determination of the total salt diffusivities and the dynamic viscosity.

Lastly, the LES model is more reliable in predicting the turbulence in the gravity current, as the buoyancy effects are not correctly captured with the $k-\epsilon$ and $k-\omega$ SST RANS models. Tuning the buoyancy constant $C_{3\epsilon}$ or modifying the buoyancy production method may improve the results of the RANS models. But when changing the domain or scale up to a lock size, extra tests are needed for the buoyancy terms of the RANS models [41].

6-2 Modeling the Bubble Screen

Simulations of the bubble screen in the fresh-fresh and fresh-salt water system are in great agreement with the lab-scale experiments and some analytical correlations. A bubble screen with a Fr_{air} in the range of 0.8 - 1.1 is found to be most efficient for mitigating salt intrusion, as was also expected from previous work at Deltares. In spite of the current results, further development is essentially required for testing the accuracy of the model.

Simulation of the Bubble Shape

When it comes to a large scale, the concentration of salts will profoundly influence the surface tension coefficient, and thus also affect the bubble shape and hence the drag coefficient. Previous work shows that the surface tension is proportional to the salt concentration, provided the concentration is not too low [31]. A concentration-dependent surface tension coefficient should be taken into consideration. Also, since the bubble diameter and the surface tension coefficient are assumed constant in the current case, so the choice of the drag model does not impact much on the validation. For further simulations, Tomiyama's model is recommended in which the drag coefficient is adjusted with varying shapes of the bubble [52]. Apart from these, the compressibility of air should be included, as the pressure difference along with the real lock height has a significant impact on the air density, and thus influence the bubble diameter and relevant parameters.

Two-Fluid Model

It is also recommended to run the simulation with the PVC tube spargers, but the inlet velocity does not meet with the actual situation with the inlet area as a slit instead of small orifices. Also, a relatively dilute plume is created by this type of sparger. A possible solution would be to use the Euler-Lagrange method, where each individual bubble is tracked throughout the computational domain [57]. A master students from TU Eindhoven, Oldeman contributed to the work on bubble screens by using this method, and got accurate results with the PVC sparger [61]. Apart from that, bubble interactions, including coalescence and break-up, need to be taken into account by possibly coupling the Euler-Euler approach with the population balance model [27].

Lab-scale Model Simulations

The present model can be extended for additional simulations. It is suggested to model the sea lock as a thin layer in the middle, as sketched in Fig.6-1. The boundary condition for the layer is set as no-slip before the bubble screen is fully developed. And then, it is converted to the interior to illustrate the opening of the lock in the fresh-salt water system. A setback is met, as shown in Appendix Fig.A-10, possibly because the set layer is thicker than expected. Moreover, different sparger types can be applied, such as a single source for bubble injection. Apart from the Froude air number, more parameters including the entrainment coefficient and the bubble screen behavior over time can be adopted both in experiments and simulations for better comparison and validation.

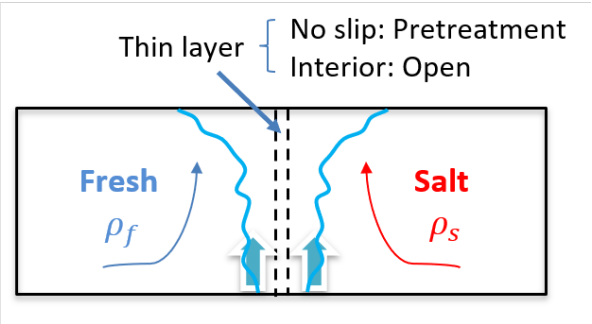

Figure 6-1: A sketch of the lock as a thin layer

Turbulence Model

Due to the limitation of Fluent, the LES model is not supported in the multiphase Eulerian model. However, the RANS approach is less reliable in predicting the gravity current and may overestimate the turbulent viscosity. A laminar model is considered for the current case. In order to fully resolve the turbulence structure in a laminar model, grid cell dimension on the orderof the Kolmogorov length scale is desired, but at a high cost of computation time. The grid size of a Taylor length scale of around 5 mm for this domain is also acceptable to partially solve the turbulent eddies. A refined grid size of around 1.3 mm is needed near the wall to predict the relevant properties of the salt tongue correctly. An alternative option would be using the multiphase mixture model with a User Defined Function (UDF) for the degassing boundary condition [52]. Another option is to develop a new solver in OpenFOAM, where the LES model can be used in the multiphase solver. Some preliminary work on programming an OpenFOAM solver for this case has been summarized in Appendix B.

Appendix A

Appendix A: Additional Results of Lab-scale Simulations

A-1 Gravity Current Results

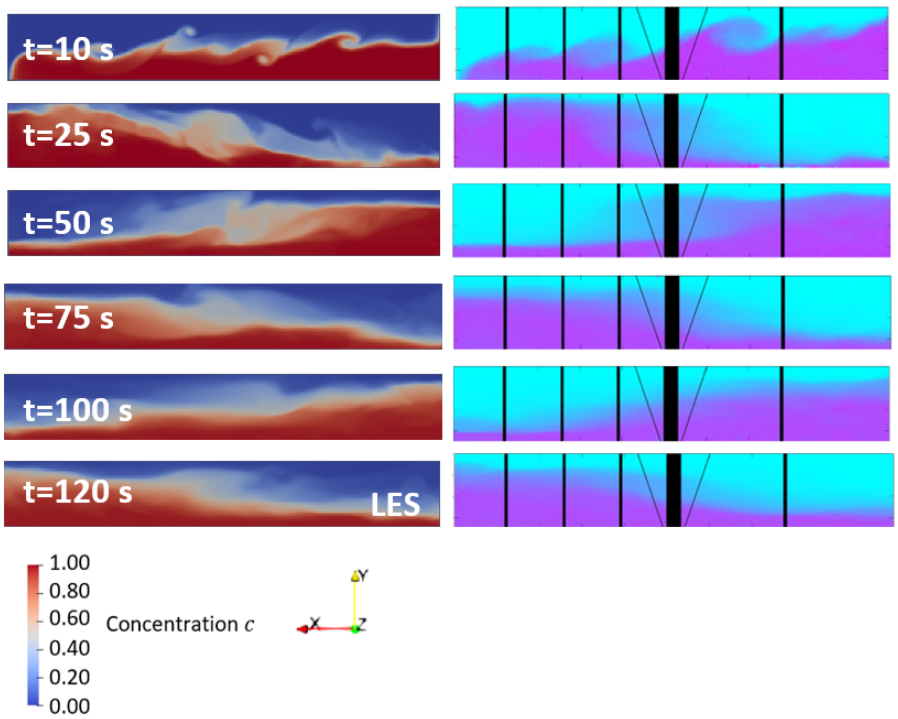

Figure A-1: Density profiles of the gravity current simulation with the LES model in the midplane $z = 0.25\ m$ (left) and the dye coloring processed images (right) at several time steps using OpenFOAM 6.

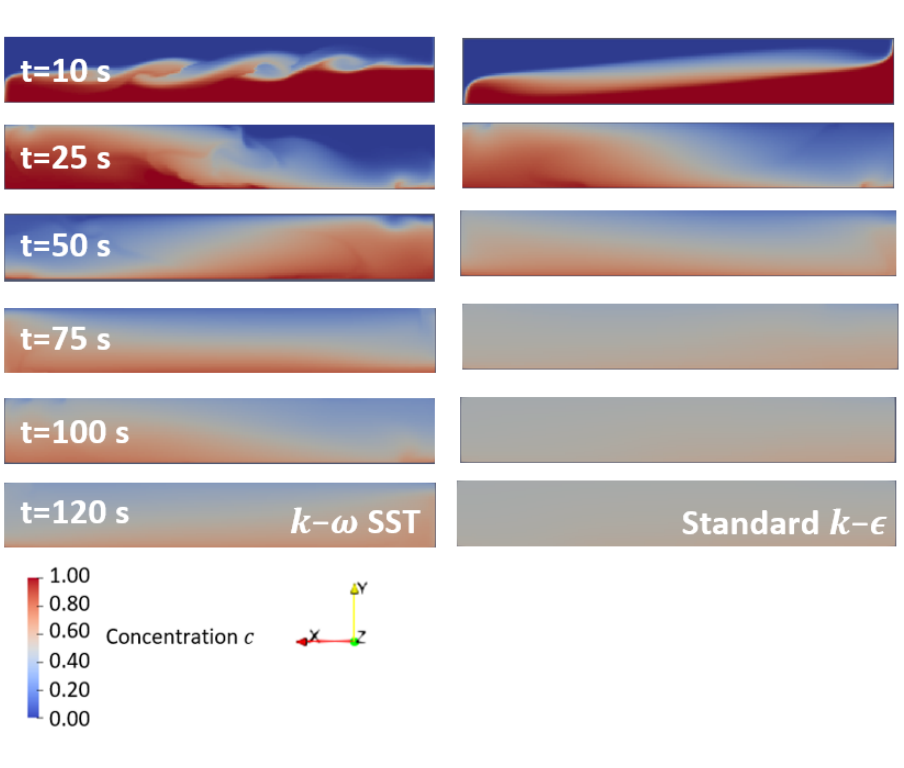

Figure A-2: Density profiles of the gravity current simulation with the $k-\omega$ SST model (left) and the standard $k-\epsilon$ model (right) in the midplane $z = 0.25\ m$ using OpenFOAM 6.

A-2 Bubble Screen In A Fresh-Fresh Water System Results

A-2-1 Turbulence Model

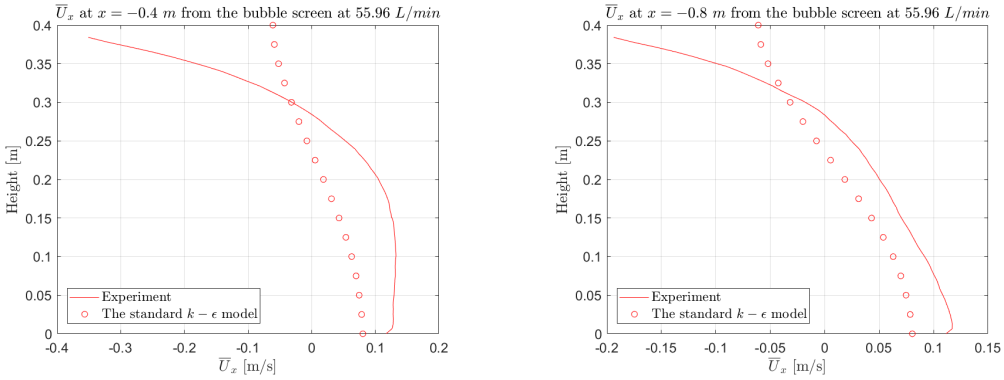

(a) Mean velocity at $x = -0.4m$ from the bubble screen.

(b) Mean velocity at $x = -0.8m$ from the bubble screen.

Figure A-3: Horizontal velocity profiles averaged over the entire $125\ s$ for $55.69\ L/min$ air flow rates in the midplane $z = 0.25\ m$ using the standard $k-\epsilon$ model in Fluent 17.2..

For the standard $k-\epsilon$ turbulence model, a large underprediction is found in the Fig.A-3 compared to the experimental results. Therefore, the buoyancy effects still plays an important role in the bubbly flow and cannot be correctly captured by the investigated RANS model. Also, it is worth noticing that the standard $k-\epsilon$ may overestimate the turbulent viscosity as a high turbulent viscosity ratio is found even at location far away from the bubble screen, whereas the turbulent viscosity is relatively low near the bubble screen.

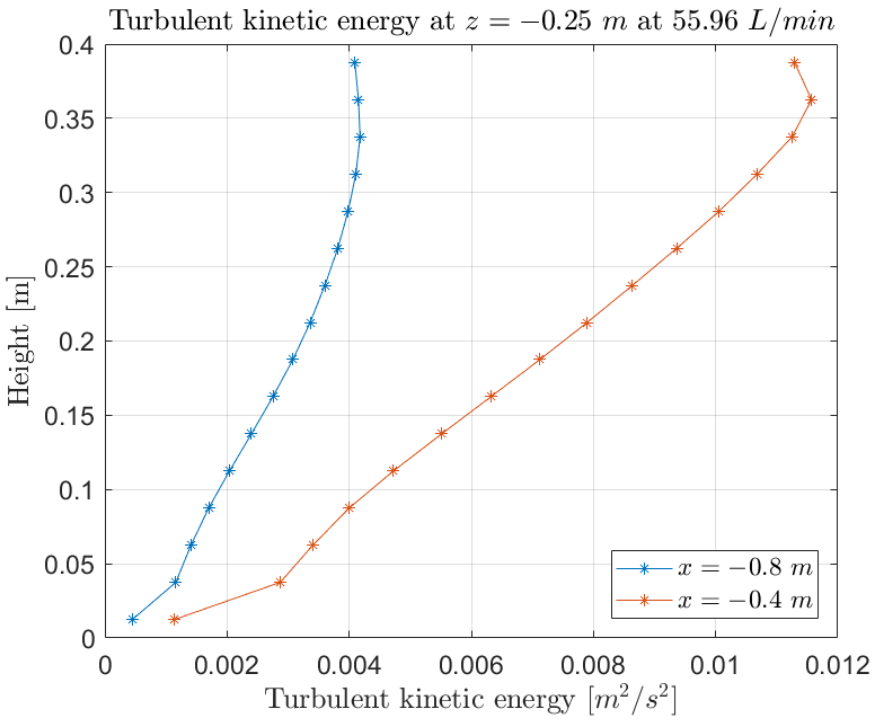

Figure A-4: Turbulent kinetic energy in the midplane $z = 0.25\ m$ at $x = -0.4\ m$ and $x = -0.8\ m$ from the bubble screen., with the air flow rate of $55.69\ L/min$ using the standard $k-\epsilon$ model in Fluent 17.2.

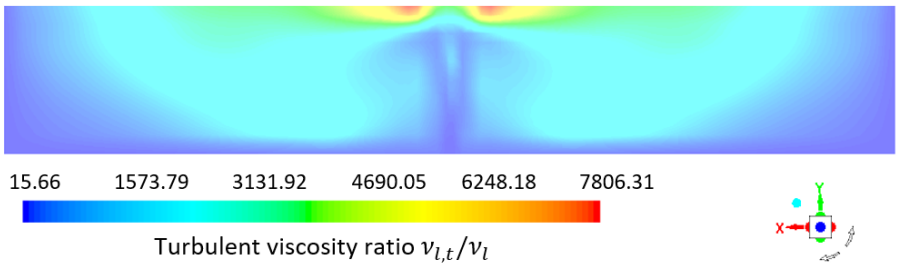

Figure A-5: Turbulent kinetic viscosity ratio in the midplane $z = 0.25\ m$, with the air flow rate of $55.69\ L/min$ using the standard $k-\epsilon$ model in Fluent 17.2.

A-2-2 Air Regeion

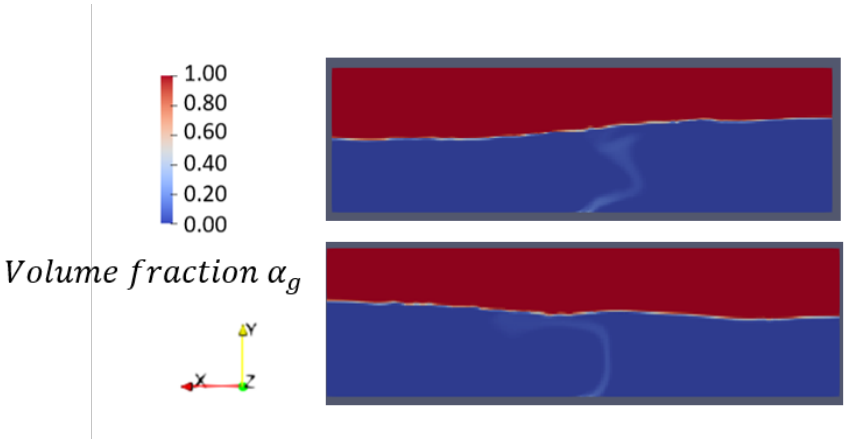

Figure A-6: A slice of the air volume fraction for two adjacent time steps, with the air flow rate of $33.50\ L/min$ using OpenFOAM 6.

A-2-3 Swaying Behavior

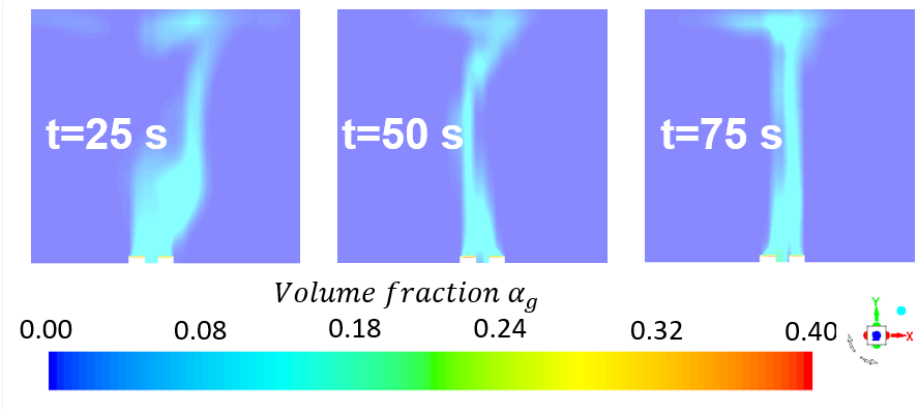

Figure A-7: A slice of the air volume fraction in the midplane at $z = 0.25m$, with the air flow rate of $55.96\ L/min$ using the "laminar" Euler-Euler method in Fluent 17.2.

A-2-4 Velocity Profiles

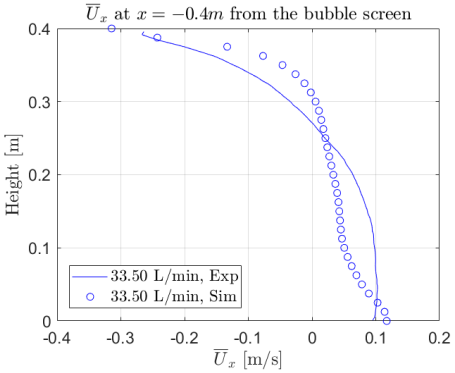

(a) Mean velocity at $x = -0.4m$ from the bubble screen.

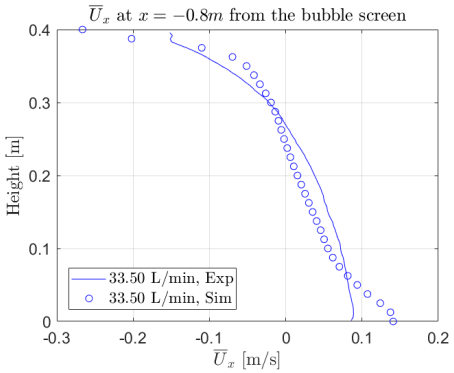

(b) Mean velocity at $x = -0.8m$ from the bubble screen.

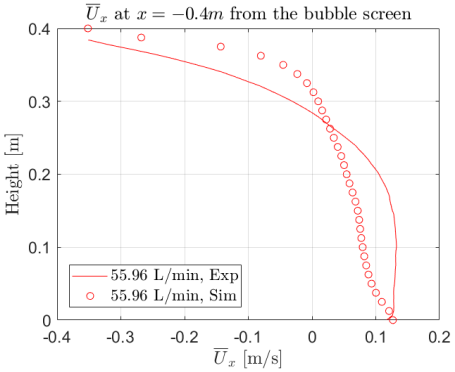

(c) Mean velocity at $x = -0.4m$ from the bubble screen.

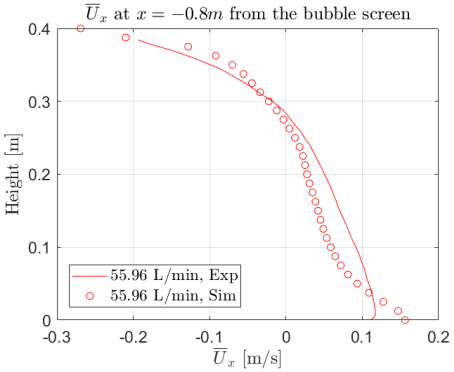

(d) Mean velocity at $x = -0.8m$ from the bubble screen.

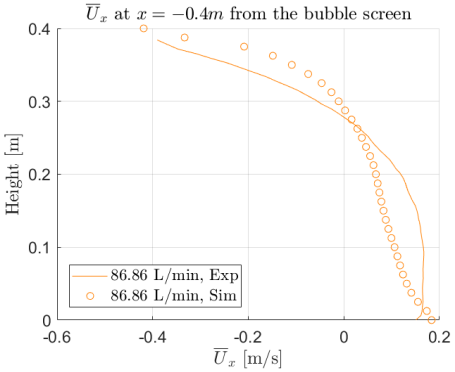

(e) Mean velocity at $x = -0.4m$ from the bubble screen.

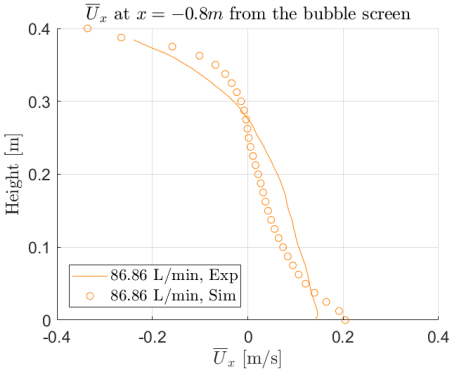

(f) Mean velocity at $x = -0.8m$ from the bubble screen.

Figure A-8: Horizontal velocity profiles averaged over the entire 125 s for each air flow rates separately in the midplane $z = 0.25$ m using the "laminar" Euler-Euler method in Fluent 17.2.

A-3 Bubble Screen In A Fresh-Salt Water System Results

A-3-1 Turbulence

For the RANS model investigated here, it is found that the standard $k-\epsilon$ model and the $k-\omega$ SST model mix the fresh and salt water in a slow fashion, which may be caused by the large underprediction as stated in Fig. A-3. It is also notable that the salt concentrations of these two models increase in a linear trend until they reach the mixing state in the end.

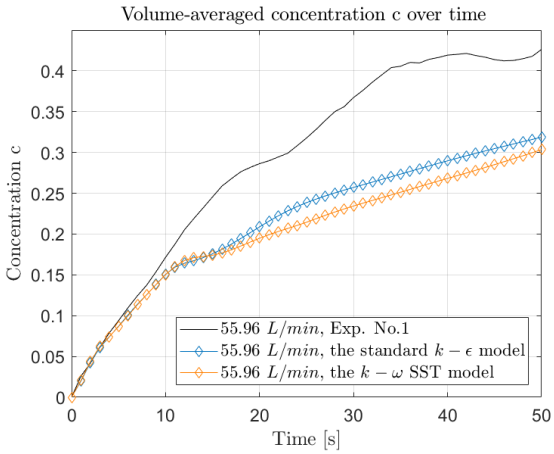

Figure A-9: Volume-averaged concentrations c over time for the standard $k-\epsilon$ mdoel and the $k-\omega$ SST model, with the air flow rate of $55.96\ L/min$ using Fluent 17.2.

A-3-2 Qualitative Analysis

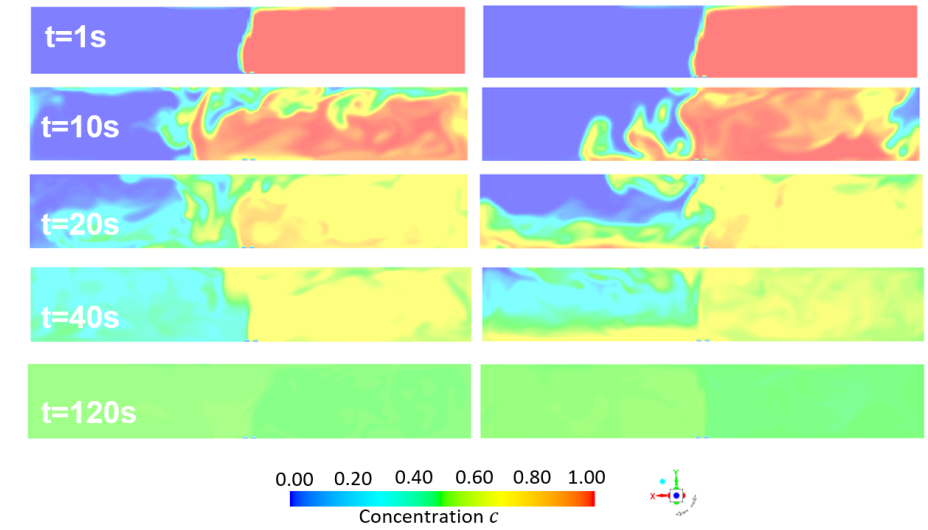

Figure A-10: The concentration profiles between 55.96 L/min (left) and 33.50 L/min (right) at several time steps in the midplane $z = 0.25m$ using the "laminar" Euler-Euler method in Fluent 17.2.

A-3-3 Mitigating Performance

Mixture Model And Lock Layer

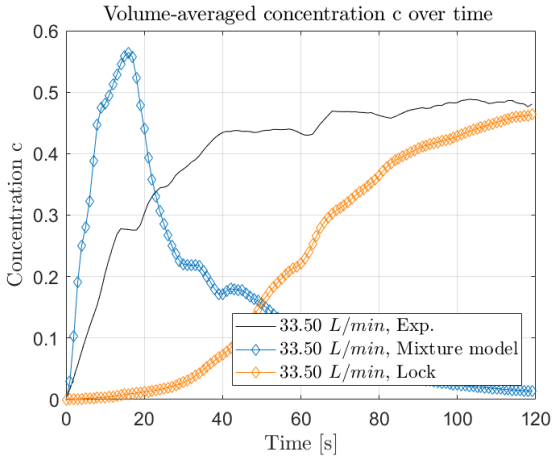

Figure A-11: Volume-averaged concentrations c over time for the mixture model with pressure outlet and the lock as a thin layer using Fluent 17.2.

PVC Tubes

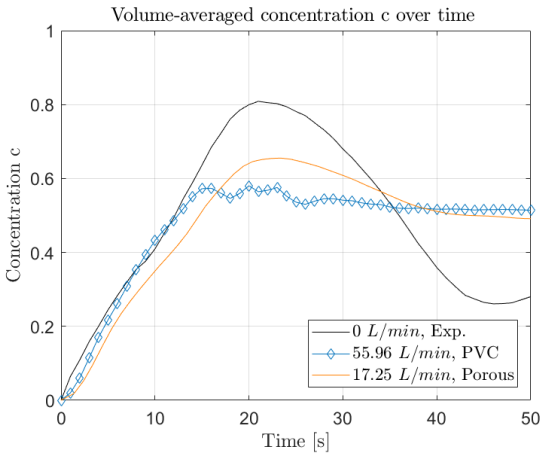

Figure A-12: Volume-averaged concentrations c over time for the first 50 s using the "laminar" Euler-Euler approach in Fluent 17.2.

A-3-4 Local Mixing Index

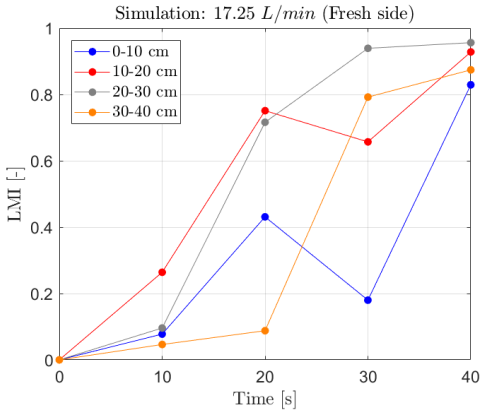

(a) air flow rate of 17.25 L/min

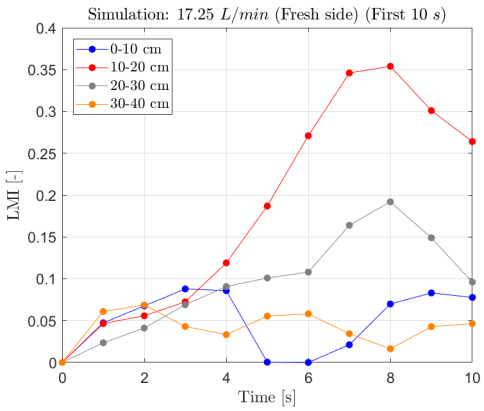

(b) air flow rate of 17.25 L/min for first 10 s

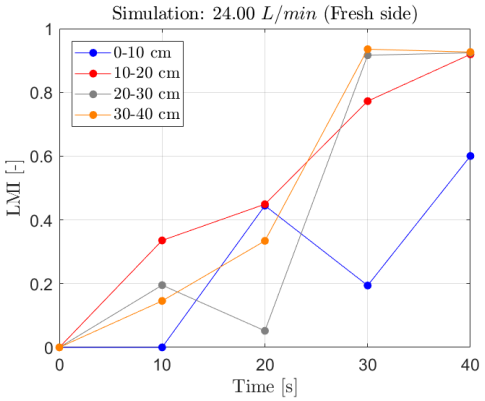

(c) air flow rate of 24.00 L/min

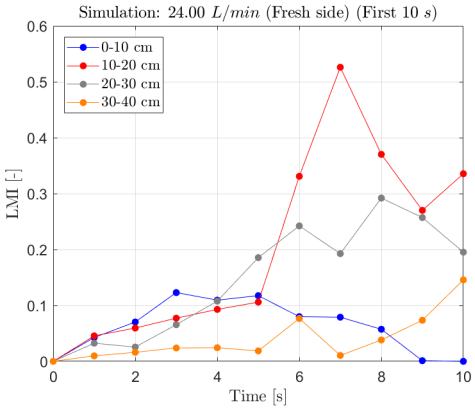

(d) air flow rate of 24.00 L/min for first 10 s

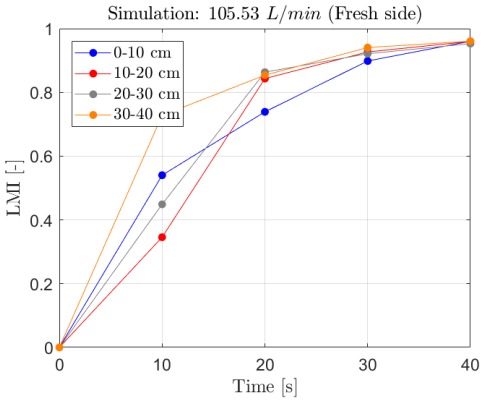

(e) air flow rate of 105.53 L/min

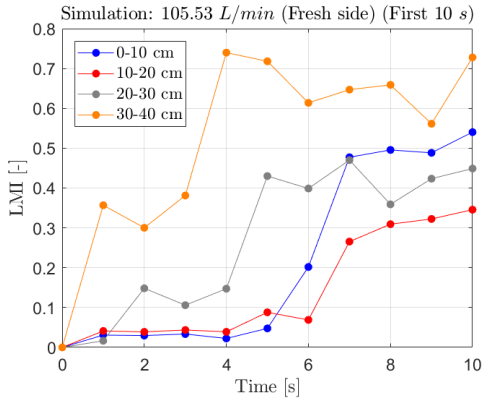

(f) air flow rate of 105.53 L/min for first 10 s

Figure A-13: The LMI over the 40 s (left) and the first 10 s on the fresh side using the "laminar" Euler-Euler method in Fluent 17.2.

Appendix B

Appendix B: OpenFOAM Simulation

B-1 Mass Transport Equation For Two-phase System

The macroscopic continuity equation for the liquid phase is expressed as:

$$\frac{\partial \rho_l}{\partial t} + \nabla \cdot (\rho_l \mathbf{u}_l) = 0 \tag{B.1}$$

with the liquid density ρ_l as a linear relation to the salt concentration:

$$\rho_l = c\rho_s + (1-c)\rho_f \tag{B.2}$$

ρ_s and ρ_f are the density of the salt water and fresh water, respectively. The following equation can be obtained by applying the volume average on Eq.(B.1) over liquid phase:

$$\frac{\partial \alpha_l < \rho_l >^l}{\partial t} + \nabla \cdot (\alpha_l < \rho_l >^l < \mathbf{u}_l >^l) - \nabla \cdot (\alpha_l D \nabla < \rho_l >^l) = 0 \tag{B.3}$$

with $< \widetilde{\rho}_l \widetilde{\mathbf{u}}_l >^l = -D\nabla < \rho_l >^l$ based on the gradient-diffusion hypothesis. $< \rho_l >^l$ and $< \mathbf{u}_l >^l$ are the intrinsic volume average of liquid density and liquid velocity, and α_l is the liquid volume concentration. Also, by appling the volume average, Eq.(B.2) is expressed as:

$$< \rho_l >^l = \rho_f + < c >^l \Delta\rho \tag{B.4}$$

with $\Delta\rho = \rho_s - \rho_f$ and $< c >^l$ is the intrinsic volume average of salt water concentration. Substitute Eq.(B.4) into the Eq.(B.3):

$$\frac{\partial \alpha_l < c >^l}{\partial t} + \nabla \cdot (\alpha_l < c >^l < \mathbf{u}_l >^l) - \nabla \cdot (\alpha_l D \nabla < c >^l) = 0 \tag{B.5}$$

Eq.(B.5) is the mass transport equation for the liquid phase that needs to be implemented into the two-phase solver in OpenFoam 6 to simulate the salt intrusion in a presence of a bubble screen.

While in Fluent 17.2, a similar equation is solved:

$$\frac{\partial \alpha_l < c >^l}{\partial t} + \nabla \cdot (\alpha_l < c >^l < \mathbf{u}_l >^l) - \nabla \cdot [\alpha_l \rho_l D \nabla (\frac{< c >^l}{\rho_l})] = 0 \tag{B.6}$$

B-2 MULES algorithm

The reactingTwoPhaseEulerFoam is the solver in OpenFOAM 6, which solves the multiphase flow in a Eulerian framework. Simply insert the mass transport equations into the solver will cause an unbounded results, as the salt concentration exceeds 1 and keeps increasing during the calculation. Therefore, the multi-dimensionsal limiter for explicit solution (MULES) algorithm, considered as a very effective method of guaranteeing boundedness of scalar fields, is applied for the implementation of the mass transport equation. Fig.B-1 provides a graphical representation of the MULES algorithm described by Peeters [8].

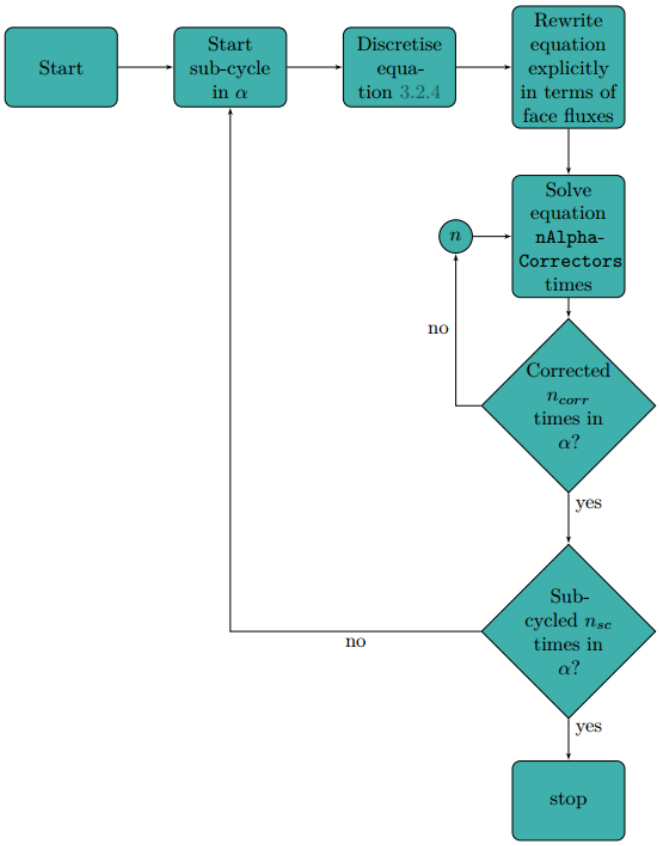

Figure B-1: Graphical representation of the MULES algorithm [8].

The solution is bounded by setting a source term S_u in the MULES method as $\nabla \cdot \mathbf{u}_l * min(c, 1)$. However, it seems that the mixing is caused by the air injection instead of the density difference according to Fig.B-2, while the density of the liquid is updated to the pressure-velocity loop for each time step.

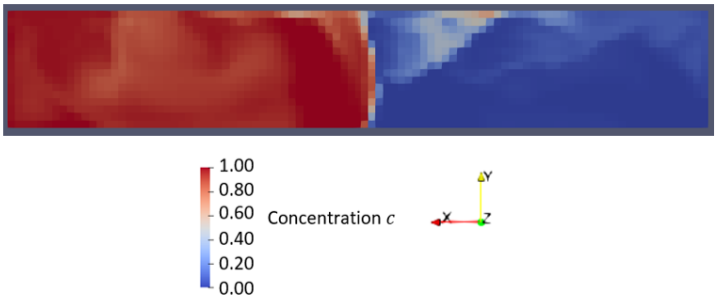

Figure B-2: Salt concentration c at $t = 8\ s$ using OpenFOAM 6.

Also, the mitigating performance simulated by the OpenFOAM 6 has a linearly increasing trend compared with the experiments. And 6% of the total salt concentration loss is found in the end.

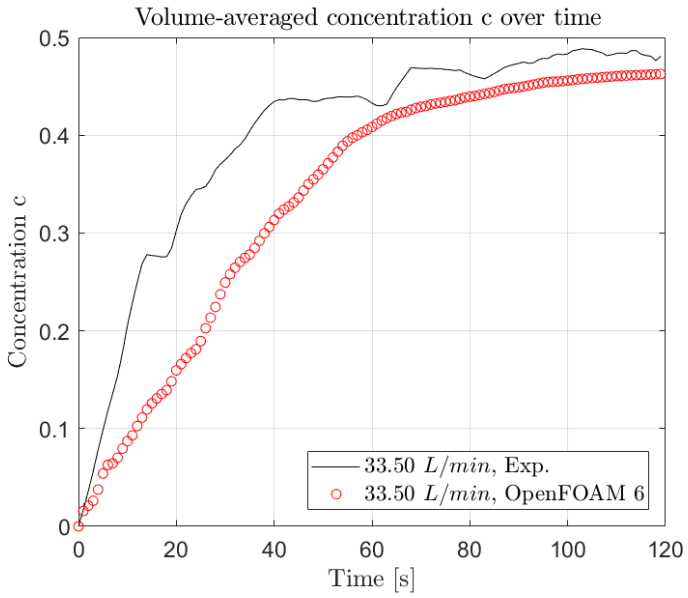

Figure B-3: Volume-averaged concentrations c over time using OpenFOAM 6.

Bibliography

[1] Y. Friocourt, T. van der Kaaij, R. Uittenbogaard, R. Plieger, and D. Verploegh, "Inzetbaarheid van luchtbellenschermen voor het beperken van de zoutindringing in de rijn-maasmonding.," *Deltares rapport 1205285-000*, 2012.

[2] G. Abraham, P. van den Burgh, and P. de Vos, "Reduction of salt water intrusion through locks by pneumatic barriers.," *Delft Hydraulics Laboratory, Publication no. 28*, 1962.

[3] J. Kurian, "Post-processing and analysis of measurements on bubble screens to mitigate salt intrusion.," *Technical report, Delft University of Technology, Deltares, Delft*, 2017.

[4] L. Nikolaidou, "Effectivity of a bubble screen as separator of waters of different densities.," *Technical report, Delft University of Technology, Deltares, Delft.*

[5] V. Wieleman, P. P. D. van der Ven, and G. Oldenziel, "Piv measurements of a bubble-screen.," *Technical report, Delft University of Technology, Deltares*, 2017.

[6] S. ten Pas, "The influence of y+ in wall functions applied in ship viscous flows.," *Marin, Internship report*, 2016.

[7] A. C. L. Nygren, "Simulation of bubbly flow in a flat bubble column.," *LUP student papers*, 2014.

[8] P. Peeters, "Cfd of multiphase pipe flow: a comparison of solvers.," 2016.

[9] B. H. Mulier, B. Veenings, G. Verbeeten, G. Wolbert, and P. V. Zaanen, "Density difference between fresh water and sea water influences the exchange mechanisms for air bubble screens.," *Technical report, Delft University of Technology, Deltares*, 2017.

[10] P. P. D. van der Ven, T. S. D. O'Mahoney, and O. M. Weiler, "Methods to assess bubble screens applied to mitigate salt intrusion through locks.," *In PIANC-World Congress Panama City, pages 1-17, Panama City*, 2018.

[11] J. O. Shin, S. B. Dalziel, and P. F. Linden, "Gravity currents produced by lock exchange.," *Journal of Fluid Mechanics, 521:1-34*, 2004.

[12] G. Abraham and P. van den Burgh, "Pneumatic barriers to reduce salt intrusion through locks.," *Rijkswaterstaat communications, no. 17*, 1973.

[13] P. S. Bulson, "Currents produced by an air curtain in deep water – report on recent experiments at southampton.," *Dock and Harbour Authority*, vol. 42, pp. 15–22, 1961.

[14] G. Keetels, R. Uittenbogaard, J. Cornelisse, N. Villars, and H. van Pagee, "Field study and supporting analysis of air curtains and other measures to reduce salinity transport through shipping locks.," *Irrigation and Drainage*, vol. 60, pp. 42–50, 2011.

[15] R. Uittenbogaard, J. Cornelisse, and K. O'Hara, "Water – air bubble screens reducing salt intrusion through shipping locks.," *36th IAHR World Congress*, 2015.

[16] R. Uittenbogaard, "Reduction of salt intrusion through shipping locks.," *PAO Stroming en Golven rond Waterbouwkundige Werken, Lecture slides*, 2015.

[17] O. Weiler, A. J. V. de Kerk, and K. J. Meeuse, "Preventing salt intrusion through shipping locks: Recent innovations and results from a pilot setup.," *36th IAHR World Congress*, 2015.

[18] J. Wen and R. S. Torrest, "Aeration induced circulation from line sources. i: Channel flows.," *Journal of Environmental Engineering*, vol. 113, pp. 82–98, 1987.

[19] I. R. Riess and T. K. Fanneløp, "Recirculating flow generated by line-source bubble plumes.," *Journal of Hydraulic Engineering*, vol. 124, pp. 932–940, 1998.

[20] P. P. D. V. D. Ven and V. A. Wieleman, "The use of small scale experiments for a shipping lock's bubble screen.," *In 4th International Symposium of Shallow Flows*, 2017.

[21] P. P. D. V. D. Ven and G. Oldenziel, "A scale model study assessing the performance of a bubble screen mitigating salinity driven lock exchange.," *5th IAHR Europe Congress*, 2018.

[22] A. Sokolichin and G. Eigenberger, "Simulation of buoyancy driven bubbly flow: Established simplifications and open question.," *AIChE Journal*, 2004.

[23] M. T. Dhotre and B. L. Smith, "Cfd simulation of large-scale bubble plumes: Comparisons against experiments.," *Chemical Engineering Science*, vol. 62, pp. 6615–6630, 2007.

[24] D. D. McClure, J. M. Kavanagh, D. F. Feltcher, and G. W. Barton, "Development of a cfd model of bubble column bioreactors: Part two - comparison of experimental data and cfd predictions.," *Chemical Engineering Technology*, vol. 37, pp. 131–140, 2014.

[25] B. Fraga, T. Stoesser, C. C. Lai, and S. A. Socolofsky, "A les-based eulerian-lagrangian approach to predict the dynamics of bubble plumes.," *Ocean Modelling*, vol. 97, pp. 27–36, 2016.

[26] S. Kamath, J. T. Padding, K. A. Buist, and J. A. M. Kuipers, "Stochastic dsmc method for dense bubbly flows: Methodology.," *Chemical Engineering Science*, vol. 176, pp. 454–475, 2018.

[27] E. Askari, OrcID, P. Proulx, and A. Passalacqua, "Modelling of bubbly flow using cfd-pbm solver in openfoam: Study of local population balance models and extended quadrature method of moments applications.," *ChemEngineering*, 2018.

[28] E. Askari, "Development, validation and application of population balance models in eulerian approach for bubbly flow reactors.," *Thèse de doctora, Université de sherbrooke*, 2018.

[29] M. V. Meerkerk and T. S. D. O'Mahoney, "Development of a cfd model of an air curtain for saltwater intrusion prevention.," *In IAHR World Congress*, pp. 1–8, 2015.

[30] Deltares, "Ontwerpstudie en praktijkproef zoutlekbeperking volkeraksluizen – beschrijving en resultaten praktijkproef stevinsluis en evaluatie maatregelen stevinsluis.," *1201226-005-ZKS-0001, version 3. Internal report. Dutch only*, 2011.

[31] M. Bostrom, D. R. M. Williams, and B. W. Ninham, "Surface tension of electrolytes: Specific ion effects explained by dispersion force.," *Langmuir*, vol. 17, pp. 4475–4478, 2001.

[32] T. B. Benjamin, "Gravity currents and related phenomena.," *Journal of Fluid Mechanics*, vol. 31, p. 209, 1968.

[33] M. I. Cantero, J. R. Lee, S. Balachandar, and M. H. Garcia, "On the front velocity of gravity currents.," *Journal of Fluid Mechanics*, vol. 586, pp. 1–39, 2007.

[34] A. Fick, "On liquid diffusion.," *Journal of Membrane Science*, vol. 100, pp. 33–38, 1995.

[35] H. Schmidt, S. Seitz, E. Hassel, and H. Wolf, "The density–salinity relation of standard seawater.," *Ocean Science*, vol. 14, pp. 15–40, 2018.

[36] S. K. Ooi, G. Constantinescu, and L. Weber, "A numerical study of intrusive compositional gravity currents.," *Phys. Fluids*, vol. 19, 2007.

[37] G. Gerber, "Experimental measurement and numerical modelling of velocity.density and turbulence profiles of a gravity current," *PhD Thesis, Stellenbosch University*, 2008.

[38] Z. Hu, X. Li, J. Yang, J. Li, and L. Wang, "Large-eddy simulation of lock-exchange gravity currents around a mounted rectangular cylinder.," *20th Australasian Fluid Mechanics Conference*, 2016.

[39] L. M. Stancanelli, R. E. Musumeci, and E. Foti, "Computational fluid dynamics for modeling gravity currents in the presence of oscillatory ambient flow.," *Water*, vol. 10, p. 635, 2018.

[40] Y. Tominaga and T. Stathopoulo, "Turbulent schmidt numbers for cfd analysis with various types of flow field.," *Atmospheric Environment*, vol. 41, pp. 8091–8099, 2007.

[41] W. Chung and C. B. Devaud, "Buoyancy-corrected k-ϵ models and large eddy simulation applied to a large axisymmetric helium plume.," *International Journal for Numerical Methods in Fluids*, vol. 58, 2008.

[42] J. Pelmard, S. Norris, and H. Friedrich, "Les grid resolution requirements for the modelling of gravity currents.," *Computers and Fluids*, vol. 174, pp. 256–270, 2018.

[43] M. Bahari, A, Hejazi, and Kourosh, "Investigation of buoyant parameters of $k-\epsilon$ turbulence model in gravity stratified flows.," *World Academy of Science, Engineering and Technology*, vol. 55, pp. 537–544, 2009.

[44] C. P. Brescianini and M. A. Delichatsios, "New evaluation of the k–ϵ turbulence model for free buoyant plumes.," *Numerical Heat Transfer*, 2003.

[45] F. R. Menter, "Two-equation eddy-viscosity turbulence models for engineering applications.," *AIAA Journal*, vol. 32, pp. 1598–1605, 1994.

[46] J. Smagorinsky, "General circulation experiments with the primitive equations.," *Monthly Weather Review*, vol. 91, pp. 99–164, 1963.

[47] P. E. Desjardin, T. J. O'Hern, and S. R. Tieszen, "Large eddy simulation and experimental measurements of the near-field of a large turbulent helium plume.," *Physics of Fluids*, vol. 16, pp. 1866–1883, 2004.

[48] E. ToolBox, "Water - density, specific weight and thermal expansion coefficient.," *https://www.engineeringtoolbox.com/water-density-specific-weight-d*$_5$*95.html*, 2003.

[49] A. Poisson and A. Papaud, "Diffusion coefficients of major ions in seawater.," *Marine Chemistry*, vol. 13, pp. 265–280, 1983.

[50] H. Anna, "Challenges in two-fluid modeling applied to large-scale bubble plumes.," *Master thesis, Dalhousie University*, 2017.

[51] L. Schiller and A. Naumann, "A drag coefficient correlation.," *Zeitschrift des Vereins Deutscher Ingenieure*, vol. 77, pp. 318–320, 1935.

[52] M. Šimcík, A. Mota, M. C. Ruzicka, A. Vicente, and J. Teixeira, "Cfd simulation and experimental measurement of gas holdup and liquid interstitial velocity in internal loop airlift reactor.," *Chemical Engineering Science*, vol. 66, pp. 3268–3279, 2011.

[53] T. F. A. Tomiyama, T. Matsuoka and T. Sakaguchi, "A simple numerical method for solving an incompressible two-fluid model in a general curvilinear coordinate system.," *Advances in Multiphase Flow*, pp. 241–252, 1995.

[54] M. L. de Bertodano, "Two fluid model for two-phase turbulent jet.," *Nuclear Engineering and Design*, vol. 179, pp. 65–74, 1998.

[55] O. Simonin and P. Viollet, "Predictions of an oxygen droplet pulverization in a compressible sub-sonic coflowing hydrogen blow.," *Numerical Methods for Multiphase Flows*, 1990.

[56] N. G. Deen, T. Solberg, and B. H. Hjertager, "Large eddy simulation of the gas-liquid flow in a square cross-sectioned bubble column.," *Chemical Engineering Science*, vol. 56, p. 6341–6349, 2001.

[57] Y. Lau, W. Bai, N. Deenn, and J. Kuipers, "Numerical study of bubble break-up in bubbly flows using a deterministic euler–lagrange framework.," *Chemical Engineering Science*, vol. 108, pp. 9–22, 2014.

[58] H. E. Kobus, "Air bubble screens as a tool for water quality control.," *Health and planning*, vol. 2, pp. 163–171, 1976.

[59] S.-H. Chou, Y.-L. Song, and S.-S. Hsiau, "A study of the mixing index in solid particles.," *KONA Powder and Particle Journal*, vol. 34, p. 275–281, 2017.

[60] P. M. C. Lacey, "The mixing of solid particles.," *Transactions of the Institution of Chemical Engineers*, vol. 21, pp. 53–59, 1943.

[61] A. M. Oldeman, "Numerical modeling of bubble screens for mitigating salt intrusion in sea locks.," 2019.